Interfacial & Nanoscale Science Facility

The Interfacial & Nanoscale Science (I&NS) Facility is a world-class resource for scientific expertise and instrumentation related to the study of interfacial phenomena and nanoscience and technology. The facility is closely aligned with the Interfacial Chemistry & Engineering (IC&E) group within the Chemical Sciences directorate of the Fundamental Science Division. This section summarizes the capabilities that exist in the I&NS facility, along with research programs associated with facility users (including the staff from IC&E). Activities in the I&NS facility and IC&E programs are jointly helping to address national needs in environmental restoration, waste management, pollution prevention, energy, and national security through research that specializes in preparation, characterization, interactions, and reactivity of interfaces and nanoscale materials. The range of scientific expertise and instrumentation within the I&NS facility provides a unique environment for research in areas such as nanoscience and nanotechnology; heterogeneous catalysis; environmental interfaces including aerosols and minerals, materials interfaces and chemoselective interfaces, and areas within microanalytical science such as chemical sensing and microfluids.

Instrumentation & Capabilities

- Thin-film deposition
- Surface analysis suite
- Electron microscopy suite
- Scanning probe microscopy
- Ion-beam processing and analysis
- Surface science and catalysis laboratory
- Catalytic reactors
- X-ray diffraction laboratory
- Microfabrication
- Other analytical and characterization laboratories

The I&NS facility provides a broad range of instrumentation, expertise and laboratory capabilities. Instrumentation is available for chemical synthesis, analytical chemistry, separations, electrochemistry, thin film deposition, catalytic reactors, ion beam processing, and microfabrication. Capabilities include an accelerator facility for material modification and analysis using ion beams along with interface characterization; scanning probe microscopies; spectroelectrochemistry; electron microscopy and x-ray analysis; high-spatial/energy resolution surface analysis; catalyst preparation, characterization and reaction engineering; a fully equipped clean room for microfabrication, microanalytical systems development and testing laboratories; inorganic, organic, polymer, and biochemical synthesis and characterization facilities; a full complement of thin film deposition and characterization facilities; and fully equipped analytical support laboratories. The combination of surface and interface characterization techniques that provide high spatial, depth, and energy resolution for a broad array of methods is unmatched anywhere in the world. Many systems are coupled directly to film growth chambers, and samples can be moved among 16 different systems under controlled environment without exposure to air.

I&NS facility staff in collaboration with members of the IC&E group continue to focus on innovative research in the areas of surface and interfacial chemistry, advanced materials synthesis and characterization, and microanalytical science. Our activities emphasize research relevant to the four DOE mission areas – basic science, energy, the environment, and national security–and operation of a world-class user facility for scientific problem solving. Our staff also plays a major role in the continued success of the EMSL by providing support, training, and collaboration to onsite users. Over the past five years, IC&E and user research activities in the I&NS facility were concentrated in four major

thrust areas: Films and Interphases, Microsensors and Microfluidics, Surface Chemistry and Catalysis, and Materials Interfaces. Staff within the I&NS facility continue to direct their efforts along these lines, with research focused in the following areas:

- Oxide and Mineral Films and Surfaces – structural and chemical properties of model single crystal oxide and complex mineral surfaces
- Electronic and Catalytic Materials – high dielectric materials, magnetic oxide semiconductors and oxide catalysts
- Nanoscale Materials – oxide quantum dots and nano films of magnetic and oxygen ion conducting oxides
- Interfacial Properties and Reactivity – reactions at oxide and mineral interfaces and the structural and chemical properties
- Microanalytical Separations and Sensing – development of new microanalytical principles, tools, and testing
- Environmental Studies – waste separations, structural and chemical stability of waste forms under different radiation and chemical environment, and atmospheric aerosols
- Analysis and Characterization – fully equipped analytical laboratories and characterization facilities.

Films and Interphases. The physical and chemical properties of the region between single phases of material (the interphase) have a major influence on many characteristics of the material, including stability, electronic properties, atomic and ionic transport, and chemical reactivity. Research programs include the synthesis of thin films and nanostructured materials, both of which contain a high concentration of interphase regions. The research activities also involve studies of solid/solid, solid/liquid and solid/gas (or vacuum) interphase regions. Although most studies are focused on inorganic materials and interphases, organic and biological systems are becoming an increasingly large part of our work.

Surface Chemistry and Catalysis. Basic research is carried out with the simplest, most well defined, environmentally relevant crystallographic structures (mineral carbonates, metal oxides) where molecular theory and spectroscopy are immediately applicable. The work then progresses to materials with more complex structures, such as iron and titanium oxides with substitutional impurities. For example, fundamental studies of the oxygen storage and release properties of pure and zirconium-doped ceria single crystal thin films are aimed at understanding how these "oxygen storage materials" perform in an automobile exhaust catalytic converter. In addition to fundamental surface chemistry research, we are developing materials and reactor designs for a number of heterogeneous catalytic processes. One study involves synthesizing, characterizing, and testing a group of novel, mesoporous silica-supported, solid-acid catalysts for use in petroleum refining processes.

Materials Interfaces. Studies are being conducted on solid/solid interfaces in a wide variety of materials, radiation effects in materials, fundamental defect properties and interactions, atomic and ionic transport, and aerosol characterization. Many of the studies on solid/solid interfaces involve 1) the characterization of interfaces between thin films and substrates, between ion-beam-modified surfaces and original substrate, or between nanoclusters and host matrices, 2) the segregation or diffusion of point defects, impurities, dopants, or gas atoms to or away from such interfaces, 3) the transport of hydrogen, oxygen, or other gases across such interfaces, 4) the formation or destruction of such interfaces from

radiation damage processes, and 5) the stability of interfaces under a wide range of environmental conditions. Studies on radiation effects include experimental research on materials for immobilization of nuclear waste and plutonium, as well as materials for next-generation nuclear power production, wide-band-gap semiconductors and multiscale computer simulations of damage production processes, defect diffusion, and microstructure evolution. Studies on atomic and ionic transport include ion exchange processes in nuclear waste glasses, hydrogen storage and transport in materials, and oxygen transport in fast ion conductors.

Microsensors and Microfluidics. Included in this work is chemical microsensor development with a focus on acoustic wave sensor arrays and optical sensing. Key areas of science in this effort include rational design of polymeric sensing materials, linear free energy models for vapor/polymer interactions, organic thin films, integrated sensor system development, and multivariate data analysis. Microfluidic analytical tools and methods are being developed in two main areas, radiochemistry and bioanalytical chemistry. Automated microanalytical separations in radiochemistry have been developed for nuclear waste characterization and medical isotope separations. Novel radionuclide sensors for water monitoring are under investigation. Bioanalytical methods are being developed for complete automated sample handling and delivery to a deoxyribonucleic acid (DNA) detector or oligonucleotide array. In addition, we are developing microfluidic renewable surface techniques as a method for observing and investigating biomolecular interactions.

Major Capabilities in I&NS Facility

Thin Film Deposition. Thin film deposition capabilities include oxygen plasma assisted molecular beam epitaxy (MBE) systems, metal organic chemical vapor deposition system (MOCVD) and sputter deposition system. MBE systems consist of growth chambers that are connected to surface characterization chambers through sample transfer lines. The growth chambers have various e-beam and effusion cell sources along with reflection high energy electron diffraction (RHEED) and quartz crystal oscillators (QCO) to monitor the growth. The surface characterization chambers are equipped with several surface science capabilities including x-ray photoelectron spectroscopy (XPS)/diffraction (XPD), Auger electron spectroscopy (AES) low energy electron diffraction (LEED), and atomic force microscopy/scanning tunneling microscopy (AFM/STM). The MOCVD system is specially designed for epitaxial growth of oxide thin films. The system comprises a rotating disk reactor, two metalorganic source delivery systems (bubbler vapor-phase and direct liquid source-injection), an oxygen microwave plasma unit, a spectroscopic ellipsometer, and a FTIR spectrometer. The system is capable of growing uniform (both thickness and composition) oxide thin films with abrupt interfaces. Sputter deposition system consists of RF and DC sputtering sources.

Surface Analysis Suite. The surface analysis suite consists of a Physical Electronics Instruments (PHI) Quantum 2000 High Resolution X-ray Photoelectron Spectrometer, a Kratos Axis Multi Technique Surface Analysis System (SAS), a PHI Model T2100 Time-of-Flight Secondary Ion Mass Spectrometer (TOF-SIMS), and a PHI Model 680 Auger Electron Spectroscopy (AES)/Scanning Auger Spectrometer (SAM). The Quantum 2000 XPS system is unique in that it uses a focused monochromatic Al K α x-ray beam that can

be varied in size from as small as 10 μm in diameter to approximately 200 μm. The TOF-SIMS system uses a pulsed and focused ion source and time-of-flight analyzer to obtain high spatial and mass resolution data from a specimen surface. The multi-technique SAS enables surfaces to be probed with a variety of complementary analysis methods and it contains electron imaging, electron spectroscopy, and both primary and secondary ion scattering capabilities. The Model 680 AES/SAM is based upon a field emission electron source and a cylindrical mirror analyzer. The electron beam size can be focused as low as 10 nm at 20 kV, although somewhat larger beams are typically used to collect AES data. Instrument features and capabilities include beam rastering, SEM imaging, mapping, a sputter gun for specimen cleaning and depth profiling, and sample rotation to allow "Zalar" rotation during sputtering. The system also is configured with an x-ray detector for near surface analysis in combination with AES surface analysis.

Electron Microscopy Suite. The electron microscopy suite consists of a LEO 982 Field Emission Electron Microscope (FESEM), High Resolution Transmission Electron Microscope, and an Environmental Scanning Electron Microscope (ESEM). The FESEM is an ultra-high performance scanning electron microscope with a resolution of 1 nm at 30 kV and 4 nm at 1.0 kV. It has a large specimen chamber equipped with multiple detectors—a below-lens secondary electron detector, an in-lens secondary electron detector, a backscatter electron detector, an energy dispersive x-ray detector, and a detector for electron backscatter diffraction. The JEOL 2010 is a high resolution TEM with a spatial resolution of 0.194 nm. This instrument has a medium acceleration voltage of 200 kV, a high brightness electron source, digital image recording, a computer-controlled sample goniometer, and a geometrically optimized x-ray detector. It has a wide range of illumination lens conditions: TEM mode, energy dispersive spectroscopy (EDS) mode, nanometer beam electron diffraction (NBED), and convergent beam electron diffraction (CBED). The TEM is post column attached with Gatan Image Filter (GIF), giving an optimized energy resolution of ~ 1.2 eV, enabling light element analysis by electron energy-loss spectroscopy (EELS) and elemental mapping in the electron spectroscopic imaging (ESI). The ESEM is a high performance, variable pressure, scanning electron microscope with a resolution of 5 nm at 30 kV. It can be used to examine uncoated, non-conductive specimens, and, with a Peltier stage, can be used with wet specimens. It will image specimens in a variety of atmospheres, such as water vapor, air, argon, nitrogen, and helium. The ESEM has a large specimen chamber equipped with an energy dispersive x-ray detector, a microinjector, and a micromanipulator.

Scanning Probe Microscopy. The scanning probe microscopy laboratory has a Digital Instrument (DI) Nanoscope IIIa AFM, A Topometrix TMX 1000 Explorer SPM, and a Park-VP scanning probe microscope. The DI Nanoscope IIIa AFM is capable of operating in both air and liquid environments and in several modes that include contact, tapping, frictional force, phase/frequency, and magnetic/electrostatic force. As a real space probe, the instrument can be used to probe surface morphology, defects, and electrostatic, magnetic, and mechanical properties of conducting and non-conducting materials. The Topometrix TMX 1000 Explorer SPM can be used for both AFM and STM in air and in liquid. This instrument includes both contact and non-contact AFM modes. STM requires an electrically conductive sample and produces images based on the topography and electronic structure of the sample. AFM samples may be insulating or conducting; the image is based on the force between the AFM probe and the sample and is primarily a map of the surface

topography. The Park-VP scanning probe microscope can be used for both STM and AFM in UHV conditions. As a real space probe, this instrument is designed to probe surface structure, defects, and morphology of conducting and non-conducting materials. In addition to STM/AFM, the vacuum system also is equipped with other surface science capabilities that include LEED, XPS, AES, and oxygen plasma cleaning.

Ion Beam Processing and Analysis. The accelerator facility is equipped with capabilities to perform material modification and analysis using high energy ion beams. The facility has two ion sources, a 3 MeV tandem ion accelerator, injector and analyzing magnets, beam lines, and four end stations. The end station on the +30° beam line is equipped with LEED, AES, XPS, oxygen plasma, and sputter cleaning sources and effusion cells in addition to the conventional ion beam capabilities. Ion beam capabilities include fixed and movable detectors for Rutherford backscattering spectrometry/Channeling (RBS/C), nuclear reaction analysis (NRA), and elastic recoil detection analysis (ERDA). This beam line extends through the end station to another end station where experiments can be performed with the beam size of 20 microns or better. The micro beam end station is also equipped with capabilities for conventional ion beam techniques including RBS, NRA, and particle induced x-ray emission (PIXE). The +15° beam line is equipped with a raster scanner for ion beam modification of materials, and the end station is equipped with all the conventional ion beam capabilities. The –15° end station is designed to carry out routine analytical work. A commercial (NEC) RC 43 end station is attached to this beam line. This end station is equipped with most of the standard ion beam analytical capabilities including RBS, NRA, PIXE, particle induced gamma emission (PIGE), and ERDA.

Surface Science and Catalysis Laboratory. Three UHV surface chemistry systems reside in the Surface Science and Catalysis Laboratory (SSCL) and are designed for studies that focus on the molecular-level chemistry of adsorbates on metal oxide surfaces. These systems are equipped with a number of spectroscopic tools to follow changes in adsorbate chemistry, including high resolution electron energy loss spectroscopy (HREELS), secondary ion mass spectrometry (SIMS), ultraviolet photoemission (UPS), XPS, AES, and LEED. In addition, both electron-stimulated (ESD) and temperature-programmed desorption (TPD) studies are routinely performed in some systems. Typical information obtainable in TPD experiments includes the quantity and nature (intact or dissociated molecule) of an adsorbed gas. In addition, an estimation of the sticking coefficient and the activation energy for desorption and/or reaction of the adsorbed molecule can be made. The system that has the combination of surface science and high pressure catalysis capabilities is capable of measuring gas/solid reaction rates under realistic, high-pressure (~1 atm) conditions using model, low surface area solid samples. Reaction rates as a function of temperature and varying reagent partial pressures can be measured in this system.

Catalytic Reactors. The Reaction Engineering Laboratories are equipped with varieties of analytical capabilities and catalytic reactors including an RXM-100 multifunctional instrument, a Zeton Altamira Reactor Test Stand. The RXM-100 is a multifunctional instrument used for catalyst studies. It combines UHV and high pressure capabilities in a single instrument without compromising specifications or ease of use. A number of measurements can be made using this instrument including chemical adsorption, physical adsorption, BET surface area, pore size, pore distribution, and temperature programmed characterization (desorption, reduction, and oxidation). An on-line mass spectrometer, gas chromatograph,

FTIR, and thermal conductivity detector can be used to analyze effluent gases. The instrument has the capability of running up to 10 different gases simultaneously. In addition, high pressure reactions (up to 1000 psi) can be run within a few minutes of each other on the same system, with little change in configuration. This system offers extensive flexibility in catalyst testing and decreases inefficiency and contamination problems that arise from transferring materials between systems and waiting for data from other sources. The Zeton Altamira Reactor Test Stand comprises three types of reactors generally used in bench scale testing of catalysts—a fixed bed reactor, Rotoberty reactor, and continuous stirred tank reactor (CSTR). This design allows users to evaluate catalyst performance and to study chemical reactions in various reactor configurations.

X-ray Diffraction. The suite of X-ray diffraction equipment in EMSL consists of four instruments: 1) a general-purpose X-ray diffraction system for studying polycrystalline samples under ambient conditions, 2) a special applications X-ray diffraction system with low-and high-temperature sample stages covering the range of -193°C to +1000°C, 3) a four-circle X-ray diffraction system, and 4) a real-time Laue camera. The general-purpose system is most often used to examine powder samples (XRPD), but can also be used to study certain types of thin films. In addition to its non-ambient capabilities, the special applications system is equipped to examine thin film samples in more detail, including grazing-incidence (GIXRD) and X-ray reflectivity (XRR) measurements. The four-circle system is typically configured for high-resolution (HRXRD) studies of epitaxial thin films. Additional applications of the four-circle system include stress measurements, texture analysis, GIXRD, and XRR. The sole application of the real-time Laue camera is to determine the orientation of bulk single-crystals, usually in concert with NMR studies.

Microfabrication. Microfabrication equipment provides a significant research and development capability in the areas of microstructures, microsensors, and microanalytical systems. Unlike highly automated industrial production equipment, this microfabrication equipment is flexible and multipurpose in function. The equipment supports a variety of microprocessing activities that include thin film deposition, thermal treatments, microphotolithography, chemical etching, inspection and characterization, bonding and packaging, and test and measurement.

Other Analytical and Characterization Laboratories. The I&NS facility has a number of wet chemistry laboratories with various capabilities including Sensor Materials Development, Chemical Microsensor Development, Vapor Generation, Calibration and Test, Microfuidic System, and Flow Injection analysis.

Capability Upgrade – 2002

Coating Capability: The Electron Microscopy suite was upgraded with an Osmium Coater, an OPC 80 Plasma Coater. To push the limits of resolution of the SEM and FESEM in the suite, the application of osmium plasma coater is crucial. As such, we decided to provide this coating capability to users of EMSL. The total expenses to establish this capability in the suite were $52,000.

BET Analysis Capability: The BET analytic needs have been increasing tremendously for the past several months. EMSL didn't have dedicated or user-friendly equipment in this area. The total expenses to establish this capability were $65,000.

Effusion Cells: State-of-the-art oxygen plasma assisted molecular beam epitaxy systems (OPA-MBE) were upgraded with additional effusion cells to meet the demand. The total expenses for this upgrade were $25,000.

Localized Reduction of Carbon Tetrachloride by Granular Iron

DJ Gaspar,[(a)] PG Tratnyek,[(b)] AS Lea,[(a)] MH Engelhard,[(a)] R Miehr,[(b)] and DR Baer[(c)]
(a) W.R. Wiley Environmental Molecular Sciences Laboratory
(b) Oregon Graduate Institute, Oregon Health & Science University
(c) Pacific Northwest National Laboratory

Granular scrap iron is being used to degrade or adsorb a variety of groundwater contaminants, including chlorinated aliphatic compounds (solvents), nitroaromatic compounds (explosives), and hazardous metals (radionuclides) (Tratnyek 1996). The environmental application of granular iron presents a complex interfacial system with a significant degree of complexity so that the relationship between different processes is highly uncertain. The overall reaction involves oxidation of the metal and reduction of an oxidant (the contaminant), but the role of reaction products and the oxide film on the metal surface have not been determined. Likewise, the question of whether contaminant reduction is dominated by reactions localized at defects in the passive film or distributed across the much larger surface area has not been answered. The uniformity or localization of reaction sites has implications for understanding and modeling the reduction of environmental contaminants by iron in ground water systems. This work (Gaspar et al. 2002) is a first attempt at determining the extent to which the metal-contaminant reaction is localized on the surface.

The OGI group reacted high purity granular iron particles (approximately 2 mm diameter) with carbon tetrachloride- (CCl_4) saturated water so that an appreciable amount of reaction product was present on the surface of the iron particles. The particles were rinsed to remove soluble reaction products such as free Cl^-, and dried. The particles were then examined, looking for a combination of structural features such as etch pits that would indicate a greater extent of reaction localized in a small region and chemical composition such as the presence of reaction products that would point to localized reaction as the source of the etch pits.

Scanning electron microscopy (SEM) revealed the presence of etch pits across the surface (Figure 1). Further measurements on a single etch pit using scanning Auger microscopy (SAM) revealed the presence of Cl inside the pit along with carbonaceous species. Analysis of a larger region using time-of-flight secondary ion mass spectrometry (TOF-SIMS) revealed widespread, but non-uniform, presence of Cl (Figure 2). These results indicate that reaction of CCl_4

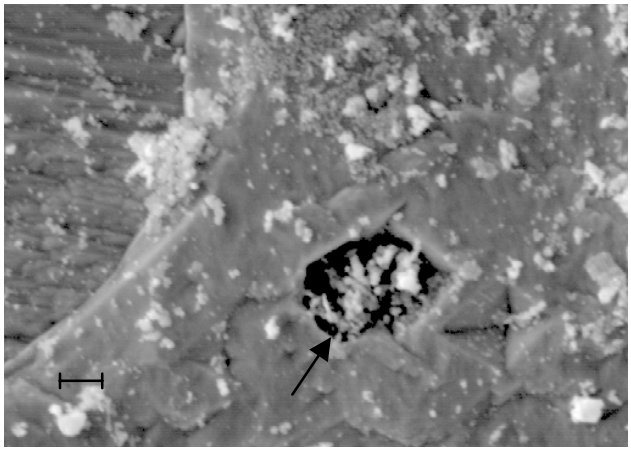

Figure 1. SEM Image of iron grain exposed to CCl_4/H_2O showing etch pit. Bar = 1 μm. The arrow points to an etch pit. From Gaspar et al. (2002).

These results indicate that reaction of CCl_4 is localized on iron particles, but not confined solely to etch pits.

The oxide film was also affected by the reaction, with X-ray photo-electron spectroscopy (XPS) analysis revealing an increase in the amount of reduced iron detected after reaction, presumably due to a decrease in the oxide film thickness, possibly near etch pits. Together the above measurements provide the first estimate of the fraction of the iron particle surface involved in the reaction with CCl_4 as between 0.3% (contribution arising from etch pits only as determined by SEM) and 18% (contribution from all surface Cl as determined by TOF-SIMS). Future work is expected to examine the conditions governing etch pit formation.

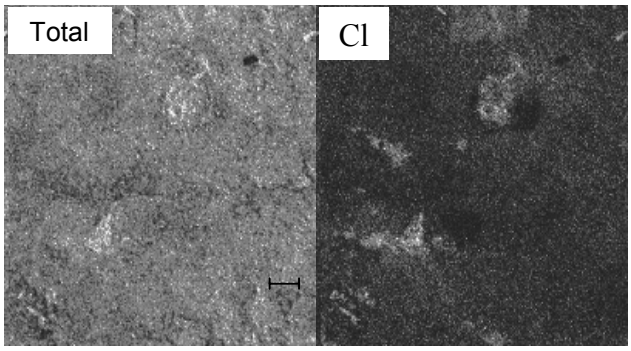

Figure 2. TOF-SIMS images of total negative and Cl^- ion signal for iron particle exposed to CCl_4/H_2O. Lighter pixels indicate higher ion signal. Image area is 100x100 μm. Bar = 10 μm. From Gaspar et al. (2002).

References

Tratnyek, PG. Putting corrosion to use: Remediating contaminated groundwater with zero-valent metals. *Chemistry and Industry,* **13**, 499-503 (1996).

Gaspar, DJ, AS Lea, MH Engelhard, DR Baer, R Miehr, and PG Tratnyek. Evidence for localization of reaction upon reduction of carbon tetrachloride by granular iron. *Langmuir,* **18,** 7688-7693 (2002).

Optimization of PZT MEMS Perfomance by Residual Stress Control

MS Kennedy,[(a)] DF Bahr,[(a)] CD Richards,[(a)] RF Richards,[(a)] LM Eakins,[(a)]
DE McCready,[(b)] and JS Young[(b)]
(a) Washington State University, Pullman
(b) W.R. Wiley Environmental Molecular Sciences Laboratory

A new Micro-Electro-Mechanical Systems (MEMS) development is the P3 microengine (Bahr et al. 2002). This device uses a composite flexing membrane to generate power by converting mechanical energy to electrical energy. The membrane is made by depositing layers of silicon dioxide, Ti/Pt, $PbZr_xTi_{1-x}O_3$ (PZT), and TiW/Au onto a micromachined boron doped silicon wafer. In order to maximize electrical output over a given pressure range, and to obtain the highest coupling coefficient, residual stresses in the membrane should be minimized. Residual stresses can also lead to material failures like cracking, buckling, and hillock formation (Thornton and Hoffman 1989).

Variations in residual stress as a function of PZT chemistry result in different pressure deflection curves (Figure 1). This was confirmed by X-ray diffraction measurements of residual stress in the PZT films (Figure 2). These data show the residual stress in the 52:48 PZT to be 350 MPa, compared to a stress in the 40:60 PZT of 160 MPa. Field-Emission Scanning Electron Microscopy (FESEM) was used to determine film thickness, and showed that processing affected the layer geometry and composition in the MEMS devices. FESEM images also revealed formation of Kirkendall voids between the Ti/SiO_2 interface (Figure 3). These voids were likely artifacts of TiO_2 formation at the Ti/SiO_2 interface, which in turn may be influenced by the large tensile stresses during processing at elevated temperatures.

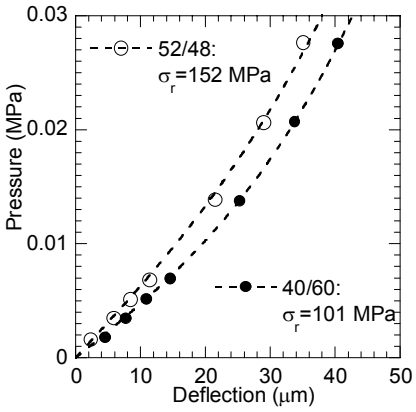

Figure 1. Pressure deflection of 52:48 and 40:60 PZT films on Si membranes.

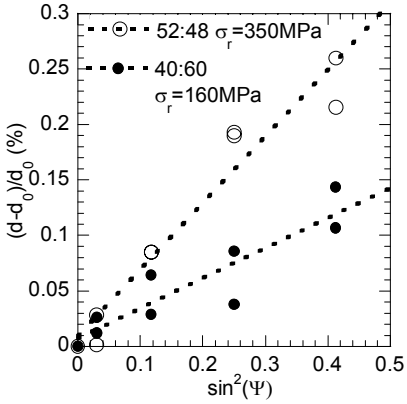

Figure 2. The slope of the plot Δd vs. sin2ψ is proportional to the stress of the PZT.

As noted, residual stress within membranes has been shown to affect deflection at a given pressure. By controlling the stress of individual layers, the overall membrane stress may be lowered. The effects of layer contribution were demonstrated by altering the Zr to Ti ratio, and thus the residual stress, of the PZT. Higher stressed 52:48 films had lower deflections than the 40:60 films at given pressures, demonstrating an increased compliance with decreasing tensile residual stress. X-ray diffraction was used to quantify the stress in the PZT films: 1.2 μm thick PZT films of

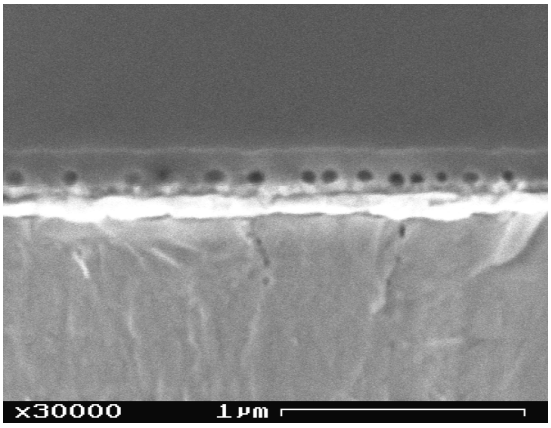

Figure 3. Formation of Kirkendall voids between the $Si0_2$ layer and the Ti.

40:60 had a tensile residual stress of 160 MPa, while a similar thickness 52:48 films showed a tensile stress of 350 MPa. Voids at the adhesion layer interface were identified, and may be impacted by stress assisted diffusion.

Acknowledgements

Financial support was provided by DARPA MTO's MicroPower Generation Program and the US Army SMDC contract #DASG60-02-C0001. Additional financial support was provided by the National Science Foundation DMI under the "XYZ on a chip" program grant #9980837.

References

Bahr, DF, KR Bruce, BW Olson, LM Eakins, CD Richards, and RF Richards, Mat. *Res. Soc. Symp. Proc.*, **687**, p.4.3.1 (2002).

Thorton, JA, and DW Hoffman. *Thin Solid Films*, **171**, 5 (1989).

Polar Oxide Interface Stabilization by Formation of Metallic Nanocrystals

V Lazarov,[(a)] SA Chambers,[(b)] and M Gajdardziska-Josifovska[(a)]
(a) University of Wisconsin, Milwaukee
(b) W.R. Wiley Environmental Molecular Sciences Laboratory

The ionic character of bonding in metal oxides significantly affects the energetics of their surfaces. Polar oxide surfaces, classified as type III oxide surfaces, have a net surface charge and an electric dipole moment in the repeat unit perpendicular to the surface, causing a divergent surface energy for bulk terminated surfaces. MgO(111) and Fe_3O_4(111) surfaces, representative of rocksalt and inverse spinel cubic structures, have been studied as model polar oxide surfaces in the search for stabilization mechanisms that remove their diverging energy. The initially accepted model of MgO(111) faceting into neutral MgO(100) surfaces is now superseded by models of MgO(111) surface reconstructions, surface metalization and hydrogen adsorption. A large relaxation has been found to stabilize Fe_3O_4(111)-1x1.

The present experimental study extends the polar surface problem to a polar interface problem, by investigating how the polarity of an oxide substrate affects the growth of polar oxide films. Single crystals of MgO, cut on the (111) plane, were selected as model polar substrates. Fe_3O_4 has a unit cell that is almost double that of the MgO cell, with a mismatch of ~ 0.33 %. Hence we have used heteroepitaxial growth to form the model Fe_3O_4(111)/ MgO(111) polar oxide interface. The results from this study will be compared against the Fe_3O_4 (111)/Pt(111) polar/metal system, and the Fe_3O_4 (100)/MgO(100) polar/neutral oxide system. In these two reference systems Fe_3O_4 has been found to grow as a pure phase in epitaxial orientation with the metal or neutral oxide substrate.

Fe_3O_4 films were grown by oxygen plasma-assisted molecular beam epitaxy (MBE) at PNNL. The films were characterized *in situ* by reflection high energy electron diffraction (RHEED) and x-ray photoelectron spectroscopy (XPS). Further *ex situ* transmission electron microscopy (TEM) characterization included bright field (BF) and dark field (DF) imaging, high resolution transmission electron microscopy (HRTEM), selected area diffraction (SAD) and convergent beam electron diffraction (CBED), performed at UWM.

RHEED was used to monitor the growth of the films, indicating that the first several monolayers grow predominantly as well ordered Fe_3O_4 epitaxial layers. Additional non-spinel reflections developed concurrently, suggesting the nucleation of secondary phases within the magnetite film. The magnetite RHEED pattern gradually faded as the growth proceeded, developing into polycrystalline ring patterns superimposed on a very weak spinel-like single crystal pattern. *In-situ* XPS from the as-grown films (Figure 1) revealed a surprising presence of Fe^0, in addition to the Fe^{2+} and Fe^{3+} peaks that were expected for Fe_3O_4. Elemental iron was not observed in XPS spectra from Fe_3O_4(100) films grown by MBE on the neutral MgO(100) surface under the same conditions used here. While the Fe^0 peaks in Figure 1 are unique identifiers of a metallic phase in the iron oxide film, a question remained whether there are other oxides present in addition to magnetite. The Fe^{2+} peak can also be indicative of FeO, while Fe^{3+} can be indicative of both the cubic and hexagonal

phases of Fe_2O_3. The chemical shifts of the oxygen peak are too small to allow the determination of iron oxide phases from XPS. Hence we undertook electron microscopy and diffraction characterization of the films.

BF-TEM (not shown) reveal an abrupt and flat film/MgO(111) interface without any signs of interface faceting into neutral MgO(100) faces. These measurements, backed by HREM observations (Figure 2), rule out interface micro- and nano-faceting as possible stabilization mechanism for this polar oxide interface system. The film surface in Figure 2 displays flat and faceted regions, but this surface morphology appears correlated with the presence of inclusions in the film.

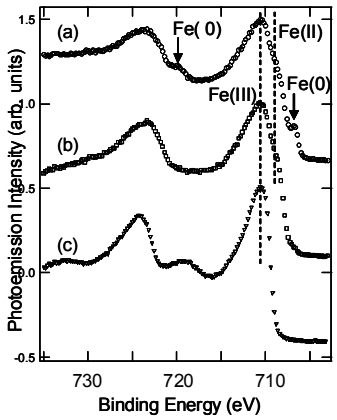

Figure 1. *In-situ* XPS of as-grown Fe_3O_4(111)/MgO(111) film showing the presence of elemental iron, Fe(0), in addition to Fe(II) and Fe(III) associated with Fe_3O_4(111) (a). Also shown are reference spectra for Fe_3O_4/MgO(001) (b), and γ-Fe_2O_3/MgO(001) (c).

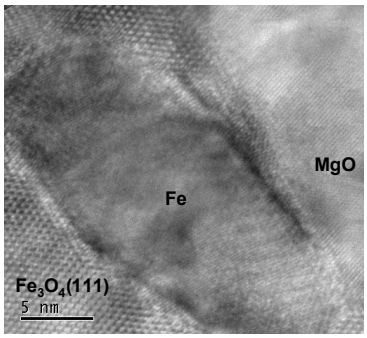

Figure 2. HRTEM image of a cross section sample showing a smaller Fe nano-inclusion nucleated on the interface and enveloped fully within the epitaxial Fe_3O_4(111) film.

Phase identification of the film and inclusions was obtained from numerical diffractograms of HRTEM images, and from electron diffraction patterns recorded with convergent and parallel illumination (CBED and SAD). Systematic CBED studies found that the majority of small inclusions and all big inclusions were elemental Fe(110), while a minority of the small inclusions were Fe_3O_4(100), which was confirmed by HRTEM and SAD data from different regions and substrate zones.

The data presented above eliminate interface faceting as a possible stabilization mechanism for this model polar oxide interface system. Instead, phase separation occurs during growth of magnetite (111) polar films on MgO(111) polar substrates, resulting in creation of majority Fe(110) and minority magnetite(100) nanocrystal inclusions. Such phase separation does not occur when polar magnetite films are grown on metal substrates and on neutral oxide substrates, suggesting that the substrate polarity is the dominant cause for the observed phase separation in the polar oxide film. Electron transfer and bond hybridization at a metal/polar-oxide interface have been proposed as mechanisms for substrate polarity reduction, as in the *ab initio* theoretical studies of Pd and Cu on MgO(111) and the experimental study of the Cu/MgO(111) interface. Such mechanisms could also drive the formation of the Fe/MgO(111) and the Fe/Fe_3O_4(111) interfaces in our system. The minority Fe_3O_4(100) inclusions appear to be a less favorable solution to the polarity problem than the Fe inclusions. Their presence within the Fe_3O_4(111) film can be rationalized from their lesser polarity, and because some of these polar magnetite (100) inclusions can nucleate on the metal Fe inclusions. The lattice mismatch of both inclusion phases with the MgO substrate and the magnetite (111) film is the most likely cause for their nano-scale dimensions, but the substrate polarity and the magnetic nature of the film and inclusions may also play a role in constraining their growth.

Al Implantation into 4H-SiC

Y Zhang,[(a)] WJ Weber,[(b)] W Jiang,[(b)] CM Wang,[(c)] V Shutthanandan,[(c)]
S Thevuthasan,[(c)] A Hallén,[(d)] and G Possnert [(d)]
(a) Ångström Laboratory, Division of Ion Physics, Sweden
(b) Pacific Northwest National Laboratory
(c) W.R. Wiley Environmental Molecular Sciences Laboratory
(d) Royal Institute of Technology, Department of Microelectronics and IT, Sweden

Success in fabricating high-quality SiC has promoted worldwide activity in establishing technologies that make a full use of this unique semiconductor. Ion implantation is the only low-temperature selective doping technique for production of SiC-based devices. There is, however, a great challenge due to inevitable production defects and lattice disorder. In collaboration with researchers at Pacific Northwest National Laboratory, much work has been devoted to studying the damage accumulation behavior of Al-implanted 4H-SiC as a function of implantation temperature, ion fluence, flux, and subsequent annealing.

Damage Accumulation

The relative disorder on both the Si and C sublattices at the damage peak for the samples implanted at 150 K is shown in Figure 1. The data indicate a predominantly sigmoidal dependence on increasing ion dose. At low ion fluences, the higher rate of C disordering is consistent with the lower threshold displacement energies and the higher production rate of C defects relative to Si defects, determined by MD simulations of energetic displacement cascades. Similar damage accumulation behavior is observed at higher implantation temperature up to 400 K.

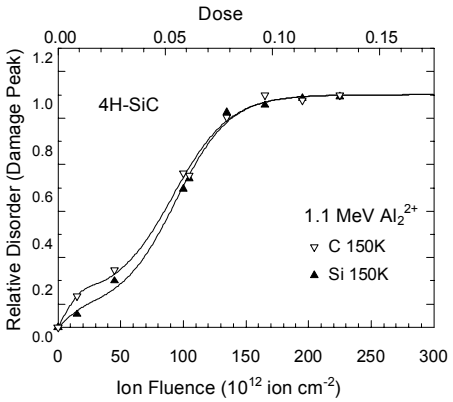

Figure 1. Relative disorder as a function of ion fluence for Al-implanted 4H-SiC.

Annealing Behaviors

Annealing behavior of the relative Si disorder under 1.1 MeV Al_2^+ implantation at 150 K is shown in Figure 2. Similar recovery behavior is observed for C sublattice. Three distinct recovery stages are observed, with the amount of specific recovery in each stage depending on the initial damage state prior to annealing. At low ion fluences (up to 1.00×10^{14} Al cm^{-2}), where the damage states are far below the fully amorphous state, recovery stages I and II are observed. At intermediate ion fluences (1.35 and 1.65×10^{14} Al cm^{-2}), where the relative disorder is just below the fully amorphous state, a distinct third recovery stage (III) is present. At high irradiation fluences, where a buried amorphous

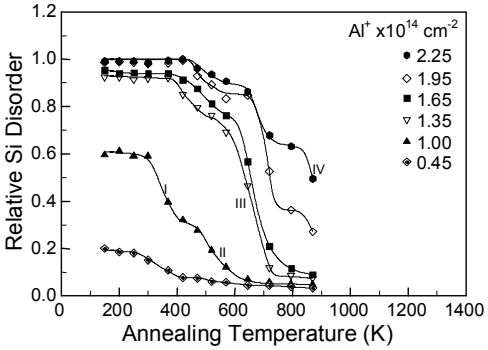

Figure 2. Isochronal recovery of relative Si disorder at the damage peak.

layer is produced (1.95 and 2.25× 10^{14} Al cm^{-2}), the onset of a fourth recovery stage (IV) is present above 800 K.

Influence of Implantation Temperature

Comparing the different disorder profiles of the 1.1 MeV Al_2^{2+} implanted samples at 150 and 450 K in Figure 3, the competing processes between the damage production and dynamic annealing is clearly demonstrated. During implantation at 450 K, dynamic recovery of interstitials and vacancies occurs at a much higher rate, which suppresses the damage accumulation; ~20 times Al fluence is tolerated compared to the 150 K case. The narrower disorder profiles for implantation at 450 K is attributed to a significant decreased local damage accumulation rate away from the damage peak and diffusion of interstitials to the planar defects in the damage peak region.

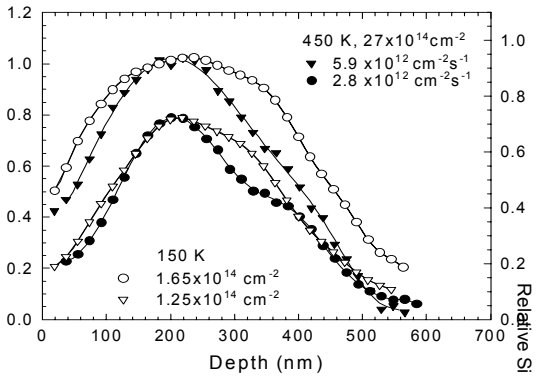

Figure 3. The relative Si disorder profiles of samples that are implanted under different temperature, ion fluence and flux. Different Y scales are used for 150 K (right) and 450 K (left) for comparison.

Ion Flux Effects

High resolution TEM (HRTEM) images (Figure 4) are taken from the damage peak region of the samples that are implanted with 1.1 MeV Al_2^{2+} to 2.7× 10^{15} Al^+ cm^{-2} at 450 K. For the low flux sample, as show in Figure 4(a), the basal plane structure is maintained, also indicated by the selected area electron diffraction (SAED) pattern, while localized strain contrast is visible. Only a few occurrences of plane bending or termination are perceived, as shown in Figure 4(b). For the high flux sample, larger linked amorphous domains are observed, as shown in Figure 4(c). The diffuse rings on the SAED pattern clearly indicate the existence of the amorphous material. The Fourier filtered image in Figure 4(d) indicates a high concentration of planar defects and a significant volume fraction of amorphous material. The planar defects appear to primarily form from the condensation of interstitials on the basal plane; however, evidence for some vacancy condensation is also observed (inset).

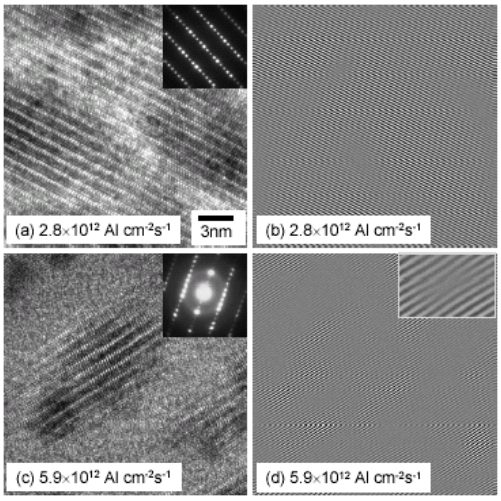

Figure 4. HRTEM micrographs of samples with different ion flux (a) and (c), as well as the corresponding Fourier filtered images (b) and (d). The insets in (a) and (c) are the corresponding SAED pattern.

Ion-irradiation of Materials Spectrally Similar to the Non-Ice Extraterrestrial Surfaces

CA Hibbitts,[(a,b)] GB Hansen,[(a,b)] T Thevuthasan,[(c)] S Shutthanandan,[(c)] TB McCord[(a,b)]

(a) Planetary Science Institute, Seattle, Washington

(b) University of Washington, Seattle

(c) W.R. Wiley Environmental Molecular Sciences Laboratory

Introduction

There are bodies in our solar system that are known as "icy" satellites, but are covered by less than 50% water-ice. Even the exposed surfaces of comets are compositionally dominated by non-ice materials. Despite the dominance of non-ice materials in the surfaces of these diverse solar system objects, most experiments and models attempting to explain surface composition have, up until now, studied the chemistry of ices and some irradiation experiments focusing on the production and trapping of volatiles in ices. However, several volatiles have recently been discovered to exist in the non-ice material on the Galilean satellites and their distributions demonstrate a clear relationship with the energetic ions trapped in the Jovian magnetosphere. The Cassini spacecraft will be able to detect this effect in Saturn's satellites and will arrive at Saturn in only 2 years. Solar flare events periodically bombard solar system objects such as our Moon, asteroids, comets, and dust with multiple-MeV protons and other ions. Space weathering is a documented fact; the possibility of space chemistry on these objects is what we intend to explore. In line with this recognition of the importance of radiogenic processing affecting the composition of non-ice materials Solar System wide, we have conducted laboratory experiments to begin the exploration of and to hopefully quantify the potentially temperature-dependent rate of *production* and *trapping* of volatiles by non-ice materials on extraterrestrial solid surfaced objects–moons, asteroids, and even Mercury. We have used terrestrial samples as analogues to the surfaces of these objects and have bombarded them with MeV hydrogen, oxygen, and sulfur ions to simulate ions trapped in the magnetospheres of Jupiter and Saturn, and in solar flare events.

Procedures

Pellets of analog extraterrestrial materials were prepared at the University of Washington from well-studied terrestrial materials including palagonite (a largely amorphous iron oxyhydroxide formed as the weathering product of basalt), montmorillonite, and serpentines (these being phyllosilicates, better known as clays). Once brought to the linear accelerator lab at PNNL they were place in the ultra-high vacuum chamber at the end of one of the ion gun beam lines, and allowed to degas. Then they were bombarded with MeV ions of H, O, and S while we measured the flux and composition of sputtered products with a quadrapole mass spectrometer.

Discussion

Mass spectra collected from background and during O^+ and O^{++} irradiations are shown in Figures 1 and 2. Mass/charge values that are invariant with sample temperature or ion dosage are due to chamber background pressure. These are the N_2^+ and N_2^{++} lines with values of 28 and 14 mass/charge ratio, and the Ar^+ line at 40. Ion bombardment can heat

the sample through ohmic heating; with the current level of the beam on the sample can exceed 1000 namps. It is also possible that the sample can be heated by chemical reactions induced through ion bombardment. We see evidence of both ohmic and chemical heating. Our primary experiment consisted of 3 runs on one sample. First, in order to avoid confusing thermal outgassing from the sample which could be possible due to ohmic heating with sputter and reaction products, we heated the sample in the chamber overnight at >100°C (for > 8 hours). We assume this desiccated and released all gasses within the top 10 microns that will be affected by ion bombardment. Because the results from this experiment are consistent with earlier results when no preliminary heating was done, we believe that thermal outgassing from even the thermally uncycled samples is minimal. Thus, we believe the release of products at greater than background levels is due directly to ion bombardment. CO_2 production (charge/mass = 44) is likely for sulfur and oxygen ion bombardment into carbon-bearing palagonite. Hydrogen and oxygen ion bombardment into pure montmorillonite or palagonite did not induce reaction products (figures not shown). The pellets tended to warm when reactions occur. Carbon was commonly sputtered. Water-products also sputter from carbon-bearing palagonite.

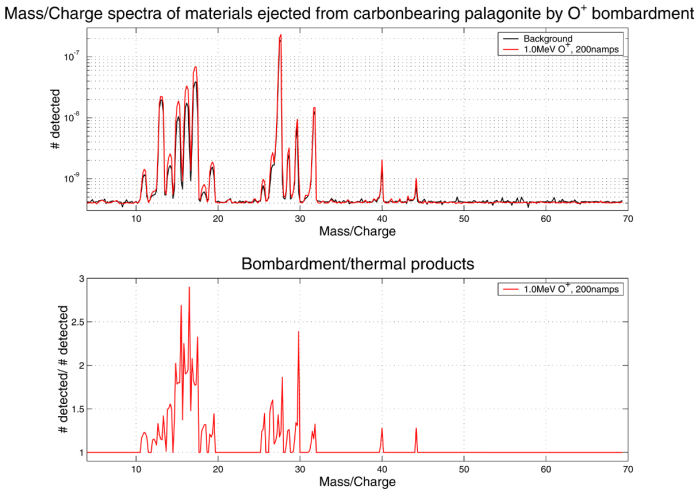

Figure 1. Very few products resulted from 200 namps bombardment with O^+. The ratio of the products/background are less than 3 and, because the Ar^+ (@ 40) peak should be independent of bombardment, much of this represents a change in background pressure. Carbon sputtering is minimal.

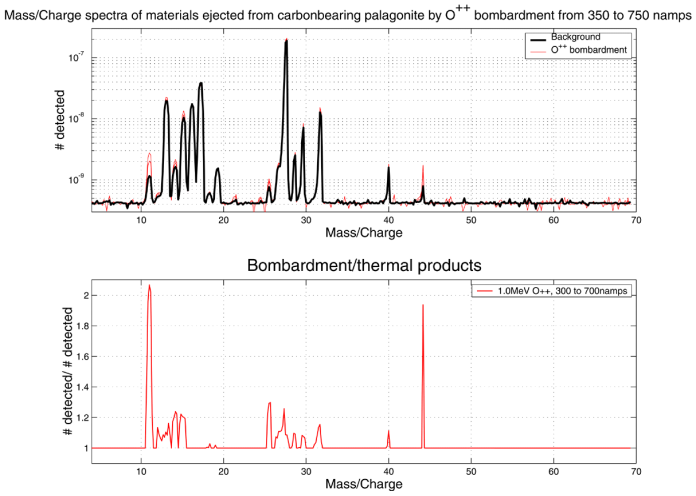

Figure 2. Again, few products result from bombardment, this time with O^{++}. Note that equivalent amperage O^+ and O^{++} equates to half the number density for O^{++}. Thus number density of ions between runs 1 and 2 are similar. The CO_2^+ peak is >> Ar^+ peak, and similar in size to the C^+ peak, and thus may be evidence of CO_2 production.

Influence of Structure and Chemistry on Piezoelectric Properties of PZT in a MEMS Power Generation Application

LMR Eakins,[(a)] DE Eakins,[(a)] MG Norton,[(a)] AS Lea,[(b)] D McCready,[(b)] J Young,[(b)] and DF Bahr[(a)]

(a) Washington State University, Pullman

(b) W.R. Wiley Environmental Molecular Sciences Laboratory

Lead zirconate titanate (PZT) is a piezoelectric oxide that has generated attention in MEMS applications. One such application transforms mechanical energy to electrical energy by flexing a PZT membrane. PZT can be deposited via solution deposition and subsequent heat treatments. The interface upon which the PZT is deposited (including internal PZT interfaces) and the stoichiometry of the solution contribute to the orientation of the resulting film. Film texture then impacts the piezoelectric properties of the oxide. The thickness of the PZT film is increased through deposition of more layers and crystallization steps. Therefore, the current study aims to elucidate the formation and contribution of the PZT/PZT interface, as well as the orientation, morphology, and chemical contributions to piezoelectric properties.

PZT films between 1 and 3 μm thick were grown using solution deposition techniques. By varying the chemistry of the film from Zr-rich to Ti-rich the film orientation increased towards {h00}. PZT with 60 wt% Ti exhibited tetragonality and produced greater electrical output at a given strain than the rhombohedral films with concentrations less than 50 wt% Ti. Multiple steps of solution deposition left identifiable PZT/PZT interfaces within the film. TEM, FESEM, and Auger spectroscopy were used to characterize these interfaces, which form upon crystallization of the amorphous PZT film. Internal PZT interfaces are associated with both structural defects (voids) as well as chemical variations such as Pb deficiencies.

Serious concerns in solution deposited PZT are chemical gradients and grain morphology. In addition to formation of harmful intermetallics and the non-piezoelectric pyrochlore phase, Pb diffusion and loss may also govern orientation and therefore electrical properties. Pyrolysis and crystallization during solution deposition become of great interest when increasing the number of deposited PZT layers since the first layers are subjected to heat treatments on every successive layer. This is when chemical gradients and PZT/PZT interfaces begin to become an issue. These processes have been found to create distinct layers in the PZT films when observed in the TEM and SEM (Tuttle et al. 1992).

AES revealed chemical gradients along the cross-section of 30 layers (~3 μm) of 52:48 and 40:60 PZT films. Figure 1 shows a reduction of Pb at points that correspond to PZT/PZT crystallization interfaces. This is further verified by AES at the film surface, which shows a reduction in Pb of about 12–15% with a concomitant increase in O. The SEM cross-section of 40:60 PZT show columnar grains within each PZT layer. However, there has been evidence of equiaxed grains in the layer nucleated at the Pt interface and columnar growth

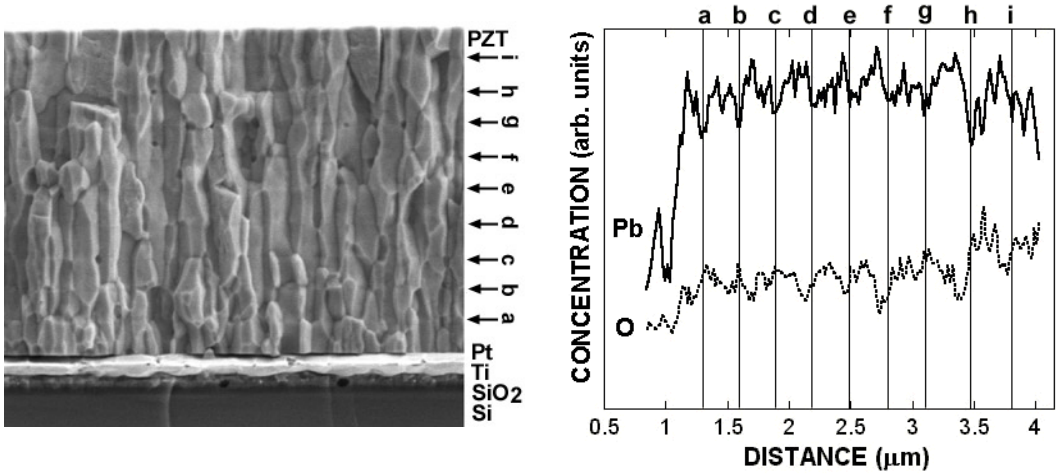

Figure 1. PZT/PZT interfaces are denoted with letters *a-i,* where *a* is the first layer deposited and *i* the last. Letters over the AES line scan denote the appropriate PZT/PZT interface.

from PZT interfaces. Many of these appear to nucleate continuous grains in subsequent layers. SEM results also support the conclusions made from TEM analysis that voiding occurs at the PZT/PZT interface in all samples although not all voiding is of the same magnitude. Presently, voiding appears to be greater in films with less crystallizations. PZT films with 30 layers (10 crystallizations), 21 layers (7 crystallizations), and 12 layers (12 crystallizations) demonstrate significantly smoother transitions between layers, with only localized voiding (i.e. some regions show no voids).

In order to determine if PZT/PZT interfaces were detrimental to output, three wafers with 3, 6, and 12 crystallizations containing 12 layers of 52:48 PZT were prepared. Crystallization after 1 and 2 layers of 52:48 PZT had specific voltages of 11.3 V/(%ε*μm) while the sample with crystallizations after 4 layers had a specific voltage of 13.7 V/(%ε*μm). The AES line scans showed significant Pb accumulation with a concomitant depletion of O near the Pt/PZT interface and surface of the PZT in the sample that underwent three crystallizations. Diffusion of Si to the Pt/PZT interface was found in the sample with six crystallizations. After 12 crystallizations, there appears to be no significant chemical gradients across the thickness. This demonstrates that fewer crystallizations yield better electrical performance regardless of large fluctuations in Pb and O.

In summary, internal PZT/PZT crystallization interfaces are visible using both SEM and TEM. These interfaces show the presence of voids on the order of tens of nanometers, as well as being deficient in Pb, as demonstrated by chemical analysis of fracture surfaces generated by *in vacuo* fracture and subsequent Auger electron spectroscopy. Minimizing the number of crystallization steps at 700°C improves the electrical output for a given PZT thickness. Pb and O chemical variations do not largely contribute to electrical integrity.

Reference

Tuttle, BA, TJ Headley, BC Bunker, RW Schwartz, TJ Zender, CL Hernandez, DC Goodnow, RJ Tissot, and J Michael. Microstructural Evolution of Pb(Zr,Ti)O_3 Thin Films Prepared by Hybrid Metallo-Organic Decomposition. *J. Mater. Res.,* **7**, 1876 (1992).

Band Offset Determination for $Sr_2TiO_4/SrTiO_3$ Heterojunctions

JH Haeni,[(a)] AM Ellis,[(a)] DG Schlom,[(a)] SA Chambers,[(b)] J Schottenfeld,[(a)] TE Mallouk,[(a)] J Robertson,[(c)] W Tian,[(d)] and XQ Pan[(d)]

(a) Pennsylvania State University, State College
(b) Pacific Northwest National Laboratory
(c) Cambridge University
(d) University of Michigan, Dearborn

Two-dimensional electron gases (2DEG) have been widely investigated in conventional semiconductors. One class of materials with properties drastically different than conventional semiconductors are perovskite semiconductors. The perovskite $SrTiO_3$, for example, has an effective mass ($m_e^* = 5m_0$) and dielectric constant (ε_r = 20,000 at 4 K) orders of magnitude higher than conventional semiconductors and the highest mobility (μ_n^{bulk} = 22,000 $cm^2/V \cdot s$ at 2 K) of any known oxide material. This completely different regime of semiconducting properties, coupled with the occurrence of superconductivity in appropriately electron-doped $SrTiO_3$, makes the study of the behavior of a 2DEG in $SrTiO_3$ of great interest.

The intrinsic properties of $SrTiO_3$, the $n = \infty$ end member of the $Sr_{n+1}Ti_nO_{3n+1}$ Ruddlesden-Popper series, are well known, and $SrTiO_3$ has been extensively studied for application to tunable dielectric devices, dynamic random access memory (DRAMs), and as an alternative gate oxide in metal-oxide-semiconductor field-effect transistors (MOSFETs). It is a metallic superconductor when doped with Nb, Ta, La, or by reduction, and has a bandgap of 3.2 eV. Unfortunately, unlike many conventional semiconductors systems, the band offset of many potential high-bandgap barrier layers with $SrTiO_3$ is unknown, making the design of an optimal 2DEG structure difficult.

We have investigated $Sr_2TiO_4/SrTiO_3$ heterojunctions, the $n = 1$ and $n = \infty$ end members of the $Sr_{n+1}Ti_nO_{3n+1}$ Ruddlesden-Popper Homologous series, respectively, as a possible system for the formation of a 2DEG in $SrTiO_3$. Sr_2TiO_4 is a particularly attractive candidate due to its excellent chemical compatibility and lattice match with $SrTiO_3$, as well as its theoretically predicted bandgap that is 0.2 eV larger than $SrTiO_3$. In this study we demonstrate the growth of epitaxial $Sr_2TiO_4/SrTiO_3$ heterojunctions by molecular beam epitaxy and the use of x-ray photoelectron spectroscopy (XPS) and diffuse reflectance to experimentally determine the band offset between $SrTiO_3$ and Sr_2TiO_4, as well as the bandgap of Sr_2TiO_4.

The valence band offset between $SrTiO_3$ and Sr_2TiO_4 was determined by comparing simulated valence band (VB) spectra, constructed by summing spectra for "bulk" (either macroscopic single crystals or thick epitaxial films) $SrTiO_3$ and Sr_2TiO_4 after weighting and shifting, with those of the actual heterostructures. Determination of the scaling factors was complicated by the fact that no unique elements were present in either heterostructure layer. As a result, the fit of the summed and heterostructure valence bands was maximized for

both valence band offsets and scaling factors. As the attenuation factor was not known *a priori*, a variety of film thicknesses were investigated to select the heterostructure with an equal contribution from the substrate and film, resulting in maximum sensitivity to the offset of one with respect to the other. Figure 1 shows a three dimensional contour plot of the χ^2 factors comparing the fit between the summed and a 30 Å thick Sr_2TiO_4 /$SrTiO_3$ heterostructure valence band spectra as a function of valence band offset and scaling factor. For each scaling factor used, a local minimum in the χ^2 values is achieved for a 0.40 eV energy shift. Analysis of the 24 Å and 38 Å thick films are in close agreement with the 30 Å film, with a valence band offset of 0.3 eV and 0.5 eV, respectively, maximizing the fit.

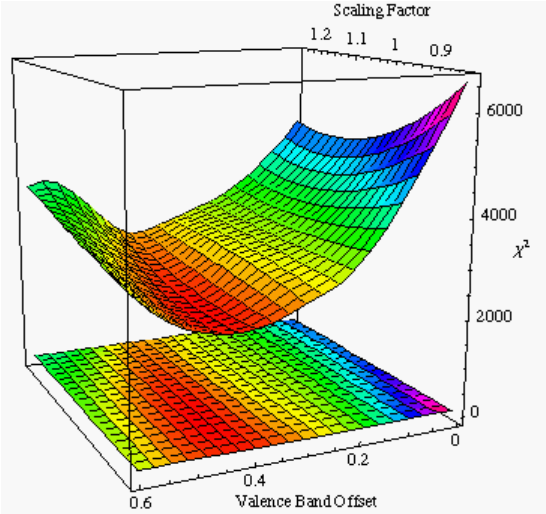

Figure 1. Contour plot of the χ^2 values indicating the fit between the 30 Å thick Sr_2TiO_4/$SrTiO_3$ heterostructure spectra and the summed $SrTiO_3$ and Sr_2TiO_4 spectra as a function of Sr_2TiO_4 spectra scaling factor (*x*-axis) and Sr_2TiO_4 energy offset (*y*-axis).

Maximized scaling factors of 1.5 for $SrTiO_3$ and 1.0 for Sr_2TiO_4 for the 24 Å thick film, and 1.0 for $SrTiO_3$ and 2.25 for Sr_2TiO_4 for the 38 Å thick film are consistent with those calculated from a first-order thickness-dependent absorption model.

The band diagram for the $SrTiO_3$/Sr_2TiO_4 heterojunction is shown in Figure 2. The materials form a type II heterojunction, with a valence and conduction band offset of –0.40 ± 0.1 eV and -0.12 ± 0.1 eV, respectively. Qualitatively, these values agree well with the theoretical band alignment that can be calculated using the model of virtual gap states. The –0.12 eV conduction band offset suggests that a heterostructure with donor doped $SrTiO_3$ and un-doped Sr_2TiO_4 may be appropriate for the creation of a confined carrier system. Activation energies of 0.08 eV for oxygen, 0.1 – 0.12 eV for La, and 0.10 eV for Nb have been reported for $SrTiO_3$, indicating that the carrier level may be sufficiently shallow in a doped-$SrTiO_3$/Sr_2TiO_4 heterostructure for carrier spillover to occur. This work represents the first step in the investigation of the fundamental materials properties and electronic structure necessary for the possible future realization of a 2DEG in such oxide heterojunctions.

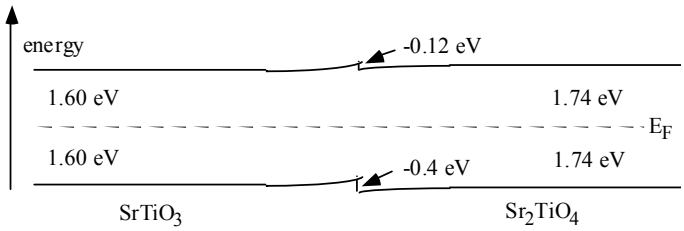

Figure 2. Band structure of a Sr_2TiO_4/$SrTiO_3$ heterojunction showing a type II band offset. Valence and conduction band offsets of –0.40 ± 0.1 eV and –0.12 ± 0.1 eV, respectively, are suggested by our experimental results.

In_2O_3/Al_2O_3 Catalysts for NOx Reduction in Lean Condition

PW Park,[(a)] CS Ragle,[(a)] CL Boyer,[(a)] ML Balmer,[(a)] MH Engelhard,[(b)] and D McCready[(b)]

(a) Caterpillar Inc., Peoria, Illinois

(b) W.R. Wiley Environmental Molecular Sciences Laboratory

A series of In_2O_3/Al_2O_3 catalysts were characterized using X-ray photoelectron spectroscopy (XPS), X-ray diffraction (XRD), and temperature programmed reduction (TPR) to better understand the surface structure of indium oxide species on the alumina support. The XRD data indicated that crystalline In_2O_3 was present at In_2O_3 loadings > 5 wt.% and the quantity of the crystalline phase increased as a function of indium loading. XPS results suggested that indium oxide existed as a well-dispersed phase up to 10 wt.% indium. The well dispersed or reducible indium oxide species below 400°C in TPR experiments were assigned as the sites which activate propene to oxygenated hydrocarbons such as acetaldehyde and acrolein. The characterization data were correlated with the catalyst performance of NOx reduction tested under lean conditions, 0.1% propene, 0.1% NOx, 9% O_2 and 7% H_2O at a space velocity of 30,000h^{-1}. The study identified that 2.5 wt.% indium was the optimum metal loading on γ-Al_2O_3, and a bifunction mechanism was proposed to explain high NOx reduction over In_2O_3/Al_2O_3 catalysts.

The intensity ratio of In $3d_{5/2}$/Al 2p calculated for theoretical atomic dispersion is also shown for comparison. The In/Al intensity ratio increased linearly with increasing In/Al atomic ratio up to 0.049 (In10) consistent with a theoretical monolayer. For higher indium loading catalysts (In15 and In20), the In/Al intensity ratios deviated from the linear trend. The In/Al intensity ratios of the catalysts which were tested for the lean NOx reaction showed similar values and a similar trend within the range of error. Therefore, exposure to reaction conditions did not affect the indium dispersion over the alumina support. The dispersions of indium species were determined by comparing the XPS intensity ratios obtained from the experiments with the values calculated from the theoretical monolayer line. The XPS results indicated that the dispersion of indium species was 100%

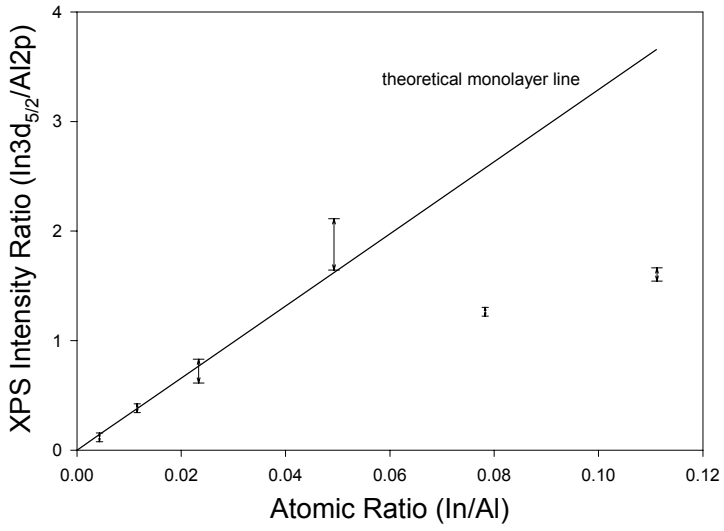

Figure 1. Variation of the XPS In3d5/2/Al2p intensity ratio measured for the In_2O_3/Al_2O_3 catalysts as a function of In/Al atomic ratio.

up to In10. However, the dispersion decreased at higher indium loading catalysts; 48 and 42% dispersion for In15 and In20, respectively.

Detectable H_2 uptake was observed at 300 and 675-700°C for In1 and In2.5 catalysts. For the higher indium loading catalysts (In5 and In10), an additional H_2 uptake peak was observed in the temperature range of 550-600°C. The H_2 consumption increased as a function of indium loading. From the comparison with the TPR spectra of standard mixtures of In_2O_3 and alumina, the H_2 uptake peaks around 550-600°C can be assigned to the reduction of the large-grained In_2O_3 crystalline phase. The H_2 uptake peak at 300°C was assigned to the reduction of the highly dispersed indium oxide species. The calculation of the amount of H_2 update for each catalyst indicated that 100% of indium oxide species were reduced to indium metal up to In5. In10 showed 83% of indium oxide to be reduced to the metal during TPR measurements.

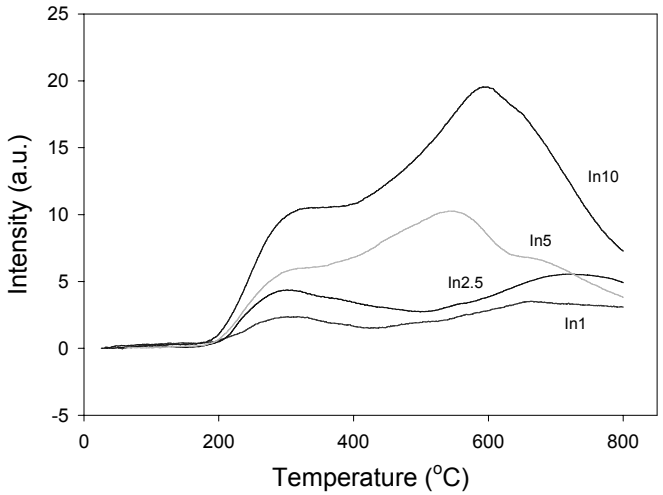

Figure 2. Temperature Programmed Reduction spectra for the In_2O_3/Al_2O_3 catalysts.

Indium (1-10 wt.% In) supported sol-gel alumina catalysts converted as high as 60% NO and 70% NO_2 to N_2 in lean exhaust conditions (1000ppm NOx, 9% O_2, 7% H_2O and 30,000 h^{-1} space velocity) with 1000ppm propene as a reductant. Optimum NOx reduction activity was achieved with 2.5wt.% indium loadings on alumina ($230 m^2/g$) prepared by a sol-gel method. The characterization and performance studies showed that it is necessary to balance the well dispersed indium species and alumina active sites in order to achieve the optimum catalytic performance. A bifunction mechanism where the indium oxide species partially oxidize propene to acrolein and acetaldehyde and the alumina utilizes the oxygenated hydrocarbons to reduce NOx to N_2 was identified. Characterization results indicated that well dispersed and readily reducible indium oxide clusters are the active sites for converting propene to the oxygenated hydrocarbons. However, the lean-NOx performance decreases at high indium loadings ($\geq$5 wt.%) where active alumina sites responsible for NOx reduction are blocked by well-dispersed indium oxide species.

Reference

Park PW, CS Ragle, CL Boyer, ML Balmer, MH Engelhard, and DE McCready. In_2O_3/Al_2O_3 catalysts for NOx reduction in lean condition. *Journal of Catalysis*, **210**, 97-105 (2002).

C and N Assimilation by Soil Microbes Studied with Time-of-Flight Secondary Ion Mass Spectrometry

JB Cliff,[(a)] DJ Gaspar,[(b)] PJ Bottomley,[(a)] and DD Myrold[(a)]

(a) Oregon State University, Corvallis

(b) W.R. Wiley Environmental Molecular Sciences Laboratory

Understanding carbon and nitrogen cycling in soils is of paramount importance if we are to understand global carbon and nitrogen cycles, optimize fertilizer use, and decipher nutrient cycling at the microbiological level. Bacteria and fungi use different sources of carbon and nitrogen depending on available resources and local conditions. One method of tracking nutrient assimilation is through the use of stable C and N isotopes.

Stable C and N isotopes have long been used to examine properties of various C and N cycling processes in soils. Unfortunately, relatively large sample sizes (typically greater than 1 cm^3) are needed for accurate gas phase isotope ratio mass spectrometric analysis. This limitation has prevented researchers from addressing C and N cycling issues on length scales relevant to bacterial metabolism ("microbially meaningful" scales, or 10–1000 μm).

To extend the use of stable isotope labeling to microbially meaningful scales, we have explored (Cliff et al. 2002) the use of time-of-flight secondary ion mass spectrometry (TOF-SIMS) to measure the incorporation of ^{13}C and ^{15}N in bacteria and fungal hyphae. In TOF–SIMS measurements, a focused $^{69}Ga^+$ beam impacts a sample surface, producing secondary ions which are mass analyzed using a TOF spectrometer, providing a mass-specific spatial map with a spatial resolution of better than 1 μm. In these preliminary measurements, we have used TOF-SIMS to detect ^{13}C and ^{15}N assimilation in a number of real and model systems.

We were able to detect ^{13}C and ^{15}N assimilation by individual bacterial cells by measuring the relative abundances of mass 26 ($^{12}C^{14}N^-$), mass 27 ($^{13}C^{14}N^-$ and $^{12}C^{15}N^-$) and mass 28 ($^{13}C^{15}N^-$) ions arising from cells adhered to a Si contact slide (Figure 1). Furthermore, we have quantified N isotope ratios in bacterial samples and individual fungal hyphae. In one such experiment, TOF-SIMS was used to locate and quantify the relative ^{15}N contents of individual hyphae that grew onto Si contact slides in intimate contact with a model organomineral porous matrix composed of kaolin, straw fragments, and freshly deposited manure, supplemented with $^{15}NO_3^-$. We observed that the ^{15}N content of fungal hyphae grown on the slides was significantly lower in regions where the hyphae

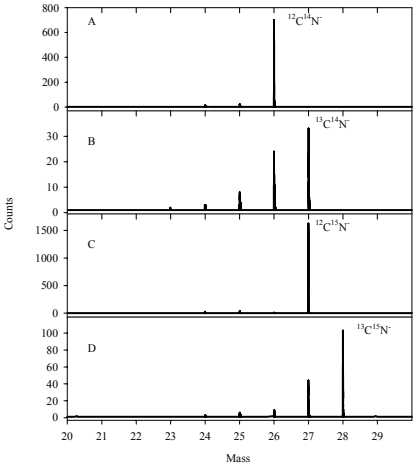

Figure 1. Partial negative TOF-SIMS spectra of *N. europaea* cells grown with $^{12}CO_2$ and $^{14}NH_4+$ (A), $^{13}CO_2$ and $^{14}NH_4+$ (B), $^{12}CO_2$ and $^{15}NH_4+$ (C), or $^{13}CO_2$ and $^{15}NH_4+$ (D) as the sole C and N sources. Figure 1 from Cliff et al. (2002).

were influenced by N-rich manure than in regions influenced by N-deficient straw. This effect occurred over distances of tens to hundreds of microns.

Amending a real clay soil with both $^{15}NH_4^+$ and $^{14}NO_3^-$ led to measurement of a soil N assimilation microsite (Figure 2). The image is an overlay of $^{27}CN^-$ ions (green) with that of $^{26}CN^-$ ions (red). The image shows a bacterium labeled more highly with ^{15}N than the fungal hypha despite the fact that the organisms are separated by less than 15 μm, demonstrating differential uptake of N-containing nutrients.

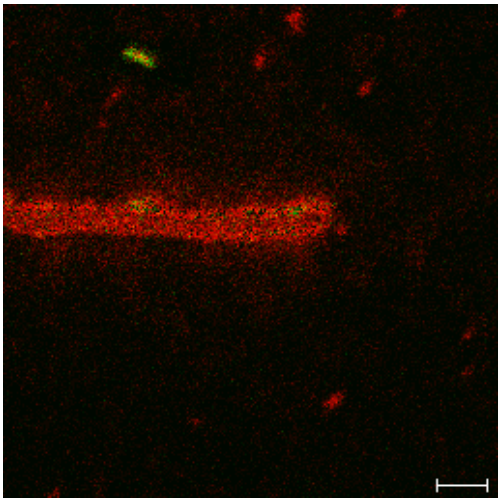

Figure 2. TOF-SIMS image of a fungal hypha and a bacterium of a Si contact slide from a clay riparian soil. The soil was labeled with $^{15}NH_4^+$ and $^{14}NO_3^-$. Red = $^{26}CN^-$, green = $^{27}CN^-$, bar = 10 μm. Figure 2 from Cliff et al. (2002).

Our data illustrate that TOF-SIMS has the potential to locate N-assimilating micro-organisms in soil and to quantify the ^{15}N content of cells that have assimilated ^{15}N-labeled nutrients and shows promise as a tool with which to explore the factors controlling microsite heterogeneities in soil. Current work is geared toward understanding the interplay between nutrient transport and microsite heterogeneities, with the ultimate goal of linking the microscale measurements reported here to meso- and macroscale understanding.

Reference

Cliff, JB, DJ Gaspar, PJ Bottomley, and DD Myrold. Exploration of inorganic C and N assimilation by soil microbes with time-of-flight secondary ion mass spectrometry. *Applied and Environmental Microbiology,* **68,** 4067-4073 (2002).

Electrochemical Sensors Based on Nanostructured Materials

Y Lin,[(a)] J Wang,[(b)] ZF Ren,[(c)] W Yantasee,[(a)] J Liu,[(d)] GE Fryxell,[(a)] and T Zemanian[(a)]
(a) Pacific Northwest National Laboratory
(b) New Mexico State University, Las Cruces
(c) Boston College, Chestnut Hill, Massachusetts
(d) Sandia National Laboratories

Nano-Composite Film of Polyaniline Nanowires and Iron (III) Hexacyanoferrate

Although oriented carbon nanotubes, oriented nanowires of metals, semiconductors, and oxides have attracted wide attention, there have been few reports on oriented polymer nanostructures such as nanowires. Recently, we developed a new approach for the assembly of large arrays of oriented nanowires containing molecularly aligned conducting polymers (polyaniline) without using a porous membrane template to support the polymer. The uniform oriented nanowires were prepared through controlled nucleation and growth during a stepwise electrochemical deposition process in which a large number of nuclei were first deposited on the substrate using a large current density. Subsequently, the current density was reduced to grow the oriented nanowires from the nucleation sites.

Nano-composite materials based on thin-films of polyaniline nanowires and iron (III) hexacyanoferrate (FeHCF) have been synthesized by electrochemical methods. The properties of the nanocomposite materials were induced by the combination of a nanoporous conducting polymer and a mixed valence compound. FeHCF nanoparticles were loaded into nanoporous polymeric matrix by an *in situ* electrochemical deposition method. The advantage of this method is that we can control the amount of FeHCF loaded into the organic polymer film. The nanoporous polyaniline PANI film has extremely high surface area and provides the excellent support for uniform dispersion of FeHCF particles in 3-D. The high surface area of nanoporous PANI film can also increase the loading capacity for FeHCF particles, which leads to the high capacity in catalysis, redox capacitors, and battery applications, and high sensitivity in chemical and biological sensing applications. The usefulness of the nanocomposites has been demonstrated with an electrochemical sensor device for H_2O_2, the detection of which is widely investigated for enzyme-based biosensors.

Biosensors Based on Carbon Nanotube Nanocomposites

We have investigated another conductive nanomaterial, carbon nanotube, for biosensor development. Carbon nanotube thin-films were immobilized on an electrode surface for biosensing. Catalytic oxidation of NADH was evaluated. The catalytic oxidation of NADH and highly stable amperometric NADH response at glassy-carbon electrodes modified with carbon-nanotube (CNT) coatings were observed. A substantial decrease in the overvoltage of the NADH oxidation reaction (compared to ordinary carbon electrodes) is observed using single-wall and multi-wall carbon-nanotube coatings. Furthermore, the NADH amperometric response of the coated electrodes is extremely stable. The CNT-coated electrodes thus allow highly-sensitive, low-potential, stable amperometric sensing. Such

ability of carbon nanotubes to promote the NADH electron-transfer reaction suggests great promise for dehydrogenase-based amperometric biosensors.

We have investigated the ability of the perfluorosulfonated polymer Nafion to solubilize single-wall and multi-wall CNT and the electrocatalytic detection of hydrogen peroxide at CNT-Nafion-coated electrodes. Nafion films have been used extensively for the modification of electrode surfaces and for the construction of amperometric biosensors owing to their unique ion-exchange, discriminative and biocompatibility properties. We have found that CNT can be suspended in solutions of Nafion in phosphate buffer. Such suspension is attributed to noncovalent interactions and permits a variety of manipulations, such as modification of electrode surfaces. The electrocatalytic properties of CNT are not affected by their association with Nafion. The resulting CNT-Nafion coated electrodes are shown to offer a marked decrease in the overvoltage (detection potential) for hydrogen peroxide. The use of Nafion as a solubilizing agent for CNT, along with the electrocatalytic detection of hydrogen peroxide, provide a useful avenue for preparing CNT-modified electrodes and suggest great promise for oxidase-based amperometric biosensors. The glucose sensor, a model biosensor, was also developed based on the immobilization of glucose oxidase-Nafion-CNT on glassy carbon and gold electrodes.

Nanoelectrode Arrays Based on Low-site Density Aligned Carbon Nanotubes

Nanoelectrode arrays (NEAs) have been successfully fabricated from the low site density aligned carbon nanotubes. The CNTs were grown by plasma enhanced chemical vapor deposition (PECVD) on Ni nanoparticles made by the electrochemical deposition. Each nanotube is separated from the nearest neighbor by several microns. NEAs consisting of up to millions of individual nanoelectrodes with diameters of 100 nm were made in a 1 cm^2 area by this non-lithography method. Electrochemical characterization, including cyclic voltammetry and square wave voltammetry, were performed. The results indicate that the carbon NEAs are promising for environmental monitoring (i.e., stripping voltammetry for trace metal analysis) and biosensing applications.

Nanoengineered Electrochemical Sensor Based on Self-Assembled Monolayers on Mesoporous Silica (SAMMS)

Various SAMMS with selective functional ligands for toxic heavy metals and actinides have been developed at PNNL. Recently we have successfully coated the SAMMS thin-films on electrode surfaces to form selective nanoengineered electrochemical sensors for detection of Cu, Cd, Pb, and Hg. The microchip gold electrode with SAMMS thin-film was integrated in a microfluidic system. Heavy metals were selectively preconcentrated on the SAMMS thin-film when sample solution continuously flowed through the electrode surface. A clean electrolyte solution was used to remove the sample matrix from the electrode surface. Square-wave voltammetry was used to quantify the surface-bound metal species. The SAMMS-based electrochemical sensors were demonstrated to be quite selective for simultaneous detection of Cu, Cd, Pb, and Hg with a detection limit at the ppb level. These results demonstrate that SAMMS-based electrochemical sensors are quite promising for toxic metal analysis.

Synthesis and TEM Characterization of One Dimensional Nano-Structured Materials

HF Zhang,[(a)(b)] LS Wang ,[(a)(b)] and CM Wang[(b)]
(a) Washington State University, Pullman
(b) W.R. Wiley Environmental Molecular Sciences Laboratory

One-dimensional quantum wires have recently attracted great interest because of the novel physics they exhibit and their potential applications as interconnects or functional components in future mesoscopic electronic and optoelectronic devices. The discovery of carbon nanotubes has significantly stimulated research activities into the syntheses and characterization of one-dimensional nanosystems. Here we report the serendipitous synthesis of Al_4C_3 nanowires and nanoribbons at mild experimental conditions using lithium as a catalyst. Large quantities of Al_4C_3 nanowires (diameters from 5 to 70 nm) and nanoribbons (5 to 70 nm thick and 20 to 500 nm wide) tens of micrometers long were synthesized in a solid-state reaction involving Al, C, Li at less than 780°C. High-resolution electron microscopy revealed that the nanowires all grew along the c-axis of hexagonal Al_4C_3 whereas the nanoribbons all grew within the basal plane. Our original goal was to synthesize solid materials containing pentatomic tetracoordinate planar carbon building blocks, (CAl_4^{2-}). Our strategy was to induce solid-state reactions in the Al/C/alkali metal tertiary systems under high temperatures, aspiring to a $M^+_2[CAl_4^{2-}]$ solid material under appropriate experimental conditions in a sealed reactor. When baking a mixture of Al-C-Li (5/3/1 atomic ratio) at 780°C for 72 hours and cooling it down rapidly to room temperature, we only observed formation of hexagonal Al_4C_3 microcrystals. However, upon slow cooling at a rate of 3°C/hour from 780°C to room temperature, we found surprisingly that a large amount of the starting material was converted into nanostructures, as revealed by scanning electron microscopy (SEM). Al_4C_3 microcrystals were still formed primarily in the initial high temperature baking at 780°C, but only in regions where there were scarce nanostructures. Two types of structures were observed, wire-like and ribbon-like, with lengths up to several tens of micrometers. The ribbon-like structures revealed by the SEM often exhibit interesting curved morphologies (Figure 1). X-ray diffraction analyses showed that the majority of the samples consisted of hexagonal crystalline Al_4C_3. Energy-dispersive x-ray spectroscopy showed that both the nanowires and nanoribbons contained primarily Al and C with a small amount of O. Electron energy loss spectroscopy confirmed this result and also showed that there was no lithium in the nanostructures.

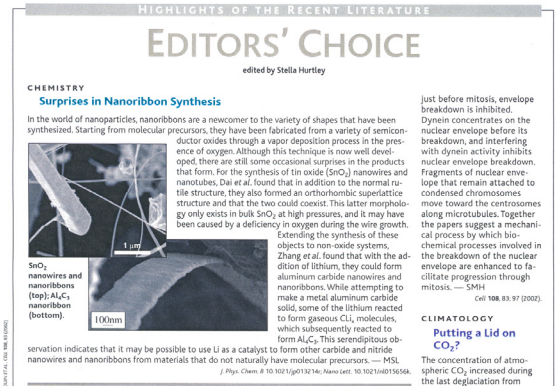
HIGHLIGHTS OF THE RECENT LITERATURE

EDITORS' CHOICE

edited by Stella Hurtley

CHEMISTRY

Surprises in Nanoribbon Synthesis

In the world of nanoparticles, nanoribbons are a newcomer to the variety of shapes that have been synthesized. Starting from molecular precursors, they have been fabricated from a variety of semiconductor oxides through a vapor deposition process in the presence of oxygen. Although this technique is now well developed, there are still some occasional surprises in the products that form. For the synthesis of tin oxide (SnO_2) nanowires and nanotubes, Dai *et al.* found that in addition to the normal rutile structure, they also formed an orthorhombic superlattice structure and that the two could coexist. This latter morphology only exists in bulk SnO_2 at high pressures, and it may have been caused by a deficiency in oxygen during the wire growth. Extending the synthesis of these objects to non-oxide systems, Zhang *et al.* found that with the addition of lithium, they could form aluminum carbide nanowires and nanoribbons. While attempting to make a metal aluminum carbide solid, some of the lithium reacted to form gaseous CLi_3 molecules, which subsequently reacted to form Al_4C_3. This serendipitous observation indicates that it may be possible to use Li as a catalyst to form other carbide and nitride nanowires and nanoribbons from materials that do not naturally have molecular precursors. — MSL

J. Phys. Chem. B 10.1021/jp013214r; *Nano Lett.* 10.1021/nl015656k.

1 μm

100nm

SnO_2 nanowires and nanoribbons (top); Al_4C_3 nanoribbon (bottom).

just before mitosis, envelope breakdown is inhibited. Dynein concentrates on the nuclear envelope before its breakdown, and interfering with dynein activity inhibits nuclear envelope breakdown. Fragments of nuclear envelope that remain attached to condensed chromosomes move toward the centrosomes along microtubules. Together the papers suggest a mechanical process by which biochemical processes involved in the breakdown of the nuclear envelope are enhanced to facilitate progression through mitosis. — SMH

Cell **108**, 83–97 (2002).

CLIMATOLOGY

Putting a Lid on CO_2?

The concentration of atmospheric CO_2 increased during the last deglaciation from

Figure 1. Al_4C_3 Nanobelts synthesized in EMSL and highlighted by editor's choice of *Science*.

Further structural characterization using transmission electron microscopy (TEM) showed that the nanowires have diameters ranging from 5-70 nm with a

mean diameter around 40 nm. Most of the nanowires were uniform in diameter along their entire length. The nanowires were all of single crystalline hexagonal Al_4C_3 with a thin Al_2O_3 layer on the outside. The oxide layer was likely formed during the TEM sample preparation and transport. High resolution TEM (HRTEM) showed that the nanowires all grew along the [0001] direction.

A variety of 1-D systems have been synthesized, including carbon nanotubes, semiconductor nanowires, coaxial nanocables, and nanobelts (Zhang 2002a, Zhang 2002b). Although helical nanostructures are common in biology or self-assembled organic systems, similar nanostructures are difficult to realize in inorganic materials. Here we report the first synthesis of helical crystalline silicon carbide nanowires covered with a silicon oxide sheath (Figure 2). Large quantities of the helical SiC/SiO_2 core-shell structures tens of micrometers long were synthesized by a chemical vapor deposition technique. The SiC core typically has diameters of 10–40 nm with a helical periodicity of 40–80 nm and is covered by a uniform layer of 30–60 nm thick amorphous SiO_2. Detailed structural characterizations suggested that the growth of this novel structure was induced by screw dislocations on the nanometer scale. Silicon carbide is a wide band-gap semiconductor and is also an important structural material. The new helical nanostructures may find applications as building blocks in nano-mechanical or electronic devices. The screw-dislocation-induced growth mechanism suggests that similar helical nanostructures of a wide range of materials may be synthesized.

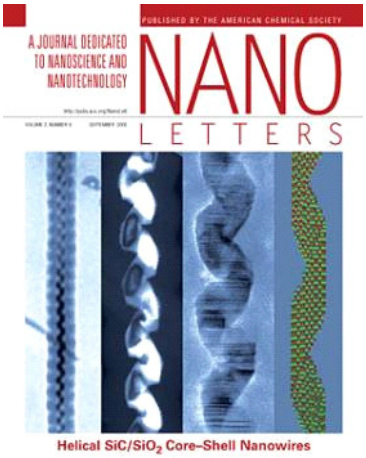

Figure 2. Helical Si/SiO_2 Core-Shell nanowires synthesized at EMSL, which is featured on the cover of *Nano Letters*.

References

Zhang, HF, AC Dohnalkova, CM Wang, JS Young, EC Buck, and LS Wang. Lithium-Assisted SelfAssembly of Aluminum Carbide Nanowires and Nanoribbons. *Nano Letters*, 2, 105-108 (2002a).

Zhang, HF, CM Wang, and LS Wang. Helical Crystalline SiC/SiO_2 Core-Shell nanowires. *Nano Letters*, 2, 941-44 (2002b).

Initial Stages of Oxidation of the Ceramic Composite ZrB_2(SiC) at High Temperature

C Tripp,[(a)] A Stephenson,[(a)] M Loeffler,[(b)] B Choi,[(c)] CV Ramana,[(a)] RJ Smith,[(a)] V Shutthanandan,[(d)] and S Thevuthasan[(d)]

(a) Montana State University, Bozeman
(b) Rhodes College, Memphis, Tennessee
(c) Jeonju University, Chonbuk, South Korea
(d) W.R. Wiley Environmental Molecular Sciences Laboratory

Zirconium-based ceramics exhibit a number of physical properties that make them interesting candidates for high temperature applications. In particular, the high melting temperature, hardness, and chemical stability of zirconium diboride ceramics make them excellent candidate materials for aerospace applications such as leading-edge components in hypersonic vehicles. The high temperature properties can be further improved by adding reinforcing phases to form metal diboride-based composites. For example, the addition of SiC particles during processing leads to improved ablation resistance at high temperature, and improved oxidation resistance.

The purpose of the present investigation was to determine the usefulness of high-energy (MeV) ion beam analysis for characterizing the early stages of oxidation of the ZrB_2-based composites. While many electron spectroscopies can be used to obtain composition vs. depth profiles with excellent depth resolution, sputter erosion for depth profiling can be very time consuming. The combination of Rutherford backscattering and nuclear reaction analysis provides relatively quick, complementary information for multiple, sequential analyses as a function of *in situ* sample treatment at high temperatures. The compromise in depth resolution inherent in MeV ion beam analysis is offset in this case by the ability to quickly obtain concentration profiles extending from the surface to a depth of several microns. An additional benefit for the samples studied here is the enhanced sensitivity to light elements obtained by using proton beams in the energy regime of enhanced non-Rutherford scattering cross sections.

In these experiments thin wafers of ZrB_2(20%-SiC) were exposed to ^{18}O gas at temperatures between 30°C and 1000°C for time periods of 30 minutes to several hours and oxygen pressures up to 4×10^{-5} Torr. The samples were cooled to room temperature for analysis. We observed that exposure of the ZrB_2(SiC) composite to oxygen under these conditions led to the reduction of ZrB_2 to form a ZrO_2 layer several microns thick at the surface. Formation of B_2O_3 was inferred from the loss of B in the surface region where the zirconium oxide forms. No evidence of silicon oxide at the surface was seen in these experiments.

The spectra in Figure 1 demonstrate the benefits of using non-Rutherford cross sections to determine the concentrations of light elements. The Rutherford cross section for B is enhanced by approximately a factor of five times the Rutherford value for 1.7 MeV protons because of nucleon-nucleon interactions. Similarly, the backscattering from oxygen at these higher proton energies is enhanced by a factor of three, depending on scattering angles. The

effects of these non-Rutherford enhancements is clearly seen in Figure 1 where the ion yields from B and O are easily seen on the background of backscattered ions from Zr. The decrease in B concentration near the surface is accompanied by the growth of an oxide layer.

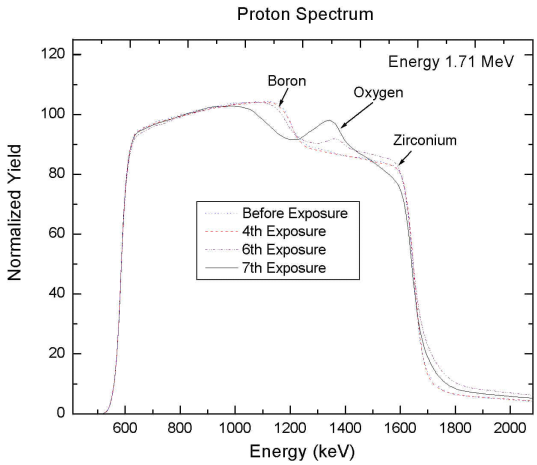

Figure 1. Backscattered ion spectrum for incident 1.71 MeV proton beam. Spectra have been normalized to the same height in the low energy region. Loss of boron and growth of oxygen is visible above the Zr background because of the enhanced, non-Rutherford scattering cross section.

Evaluation of Large-Area Filtered Arc Deposition Technology for Corrosion Resistant Coatings on Interconnct Plates for Solid Oxide Fuel Cells

RJ Smith,[(a)] CV Ramana,[(a)] Vladimir Gorokhovsky,[(b)] V Shutthanandan,[(c)] and S Thevuthasan[(c)]

(a) Montana State University, Bozeman
(b) ARCOMAC Surface Engineering, Inc., Bozeman, Montana
(c) W.R. Wiley Environmental Molecular Sciences Laboratory

The goal of this project is to determine the feasibility of using the large-area filtered arc plasma source ion deposition technology (LAFAD) for the production of corrosion-resistant bipolar plates in planar solid-oxide fuel cells (SOFC). The need to reduce costs for components in the SOFC suggests using inexpensive metallic alloys for the interconnecting plate between adjacent cells in a SOFC stack. Most metals will fail quickly due to corrosion in the high-temperature, gaseous environment of the cell, resulting in potentially catastrophic gas leaks. Multilayer coatings on these plates are proposed as a solution to provide oxidation resistance and chemical stability with adjacent components, while maintaining good through-plane electrical conductivity. Good bonding characteristics and integrity of the coatings against thermal cycling (>800°C) are also required. The capability for LAFAD to grow extremely smooth surfaces of multi-layer coatings with a low pinhole density is being used to design coatings with the desired properties. The corrosion resistant coatings will be optimized as a function of several deposition parameters, including substrate material, surface preparation, substrate temperature, number and composition of individual layers, and addition of ultra-thin diffusion barriers. The physical, chemical, and electrical integrity of the coated plates is then tested as a function of time at a typical operating temperature in oxidizing conditions.

In these initial experiments, multi-layer coatings of CrN and AlN were fabricated on steel discs using LAFAD at Arcomac Surface Engineering, Inc. Nitrides were selected because of their excellent wear resistance. Furthermore, AlN is oxidation resistant while CrN is a good electronic conductor. The composition-depth profiles were measured using Rutherford backscattering in the ion beam facilities at EMSL. Nuclear reaction analysis using a beam of 0.94 MeV D^+ was performed to determine the total N and O concentration in the coatings as a function of annealing time at 1073 K. We observed that a relatively thick

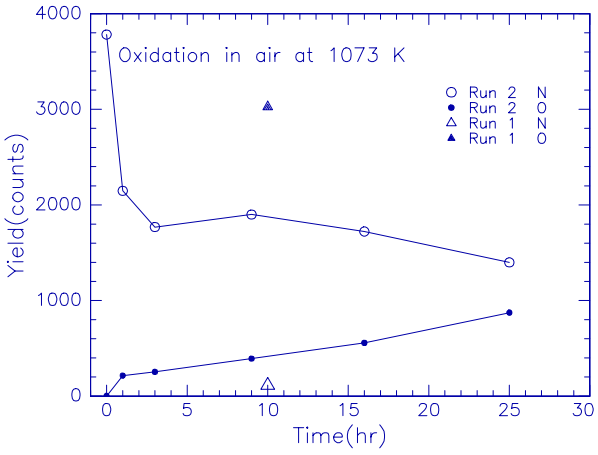

Figure 1. Concentration of oxygen and nitrogen, measured by NRA, in thin coatings deposited using LAFAD.

multilayer coating of CrN/AlN (Run 1 in Figure 1) was completely oxidized following annealing for 10 hours 1073 K. Very little nitrogen remained in this film. A second multilayer structure (Run 2 in Figure 1) was designed with different layer thicknesses to exploit the oxidation resistance of AlN. This structure was annealed at 1073 K for a total of 25 hours. Ion beam analysis showed considerable improvement in oxidation resistance, as shown in Figure 1. The concentration of N (open circles) is observed to decrease and saturate at a reduced value. Similarly, oxidation (closed circles) proceeds at a remarkably slower rate than that for Run 1. Ongoing work in 2003 will focus on the role of layer composition and thickness in enhancing oxidation resistance while maintaining electrical conductivity.

Measurement of Arsenic Concentration in an Adsorbent Using Proton Induced X-Ray Emission (PIXE)

S Maheswaran,[(a)] V Shutthanandan,[(b)] and S Thevuthasan[(b)]

(a) University of Western Sydney

(b) W.R. Wiley Environmental Molecular Sciences Laboratory

Quantification of trace metals in any adsorbent directly with high accuracy and sensitivity is a challenging task. High-energy ion beam based proton induced x-ray emission (PIXE) spectroscopy is an effective technique for sensitive and quantitative analysis of trace elements in materials. We have used PIXE to quantify the ppm level of arsenic adsorbed in powder activated carbon (PAC) during the exposure of PAC to arsenic solutions. In general, PAC with a 150 μm particle size has been effectively used as an adsorbent to remove arsenic from drinking water.

To evaluate different aspects of adsorption mechanisms in PAC, we have carried out equilibrium and kinetic adsorption experiments. After the exposure, arsenic concentration in the adsorbent was quantified using PIXE with a 0.5 mm ion beam, and these results were compared to the inductively coupled plasma (ICP) measurements.

Figure 1 shows the results of equilibrium experiments in which different amounts of PAC (from 0.1–5.0 g/L) were added to a solution with an initial arsenic concentration of 1.0 mg/L and then mixed on a platform mixer for 72 hours. After the treatment, the PAC was isolated from the solution and As concentration in PAC was measured directly using PIXE. To determine As concentration in PAC, ICP measurements were also carried out after stripping all the As from PAC (ICP-direct). The concentration of remaining As in treated solution was measured using ICP. The amount of arsenic adsorbed by PAC (O ICP) was calculated by subtracting from the amount of arsenic present in the initial solution.

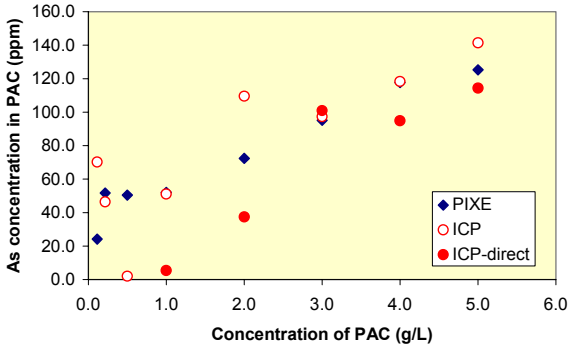

Figure 1. PIXE and ICP measurements of arsenic concentration in PAC after the equilibrium experiment.

Figure 2 shows the results of kinetic experiments in which 5g/L of PAC was added to a solution with an initial arsenic concentration of 1.0 mg/L and then agitated for between 5 minutes and 8 hours. After the treatment, the PAC was isolated from the solution and As concentration in PAC was determined using PIXE and ICP measurements.

The differences observed between these two measurements are mainly due to inhomogeneous structure of PAC. This includes the variable surface properties such as surface area and pore sizes in each particle. Some differences between ICP measurements are also clearly visible. The variation of As absorption in the PAC was further investigated by micro-beam PIXE using a 20 micron proton beam. Arsenic concentration maps of two different PAC particles obtained using micro-beam PIXE measurements are shown in Figure 3. It is clear from these pictures that the As absorbed non-uniformly within the PAC particle. In addition, the As concentration varies significantly between these two particles. Arsenic adsorption characteristics of PAC can be studied by fitting these experimental data with various theoretical models.

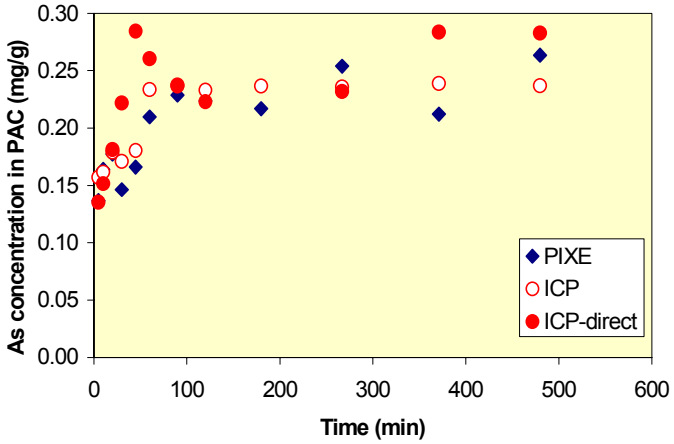

Figure 2. PIXE and ICP measurements of arsenic concentration in PAC after the kinetic experiment.

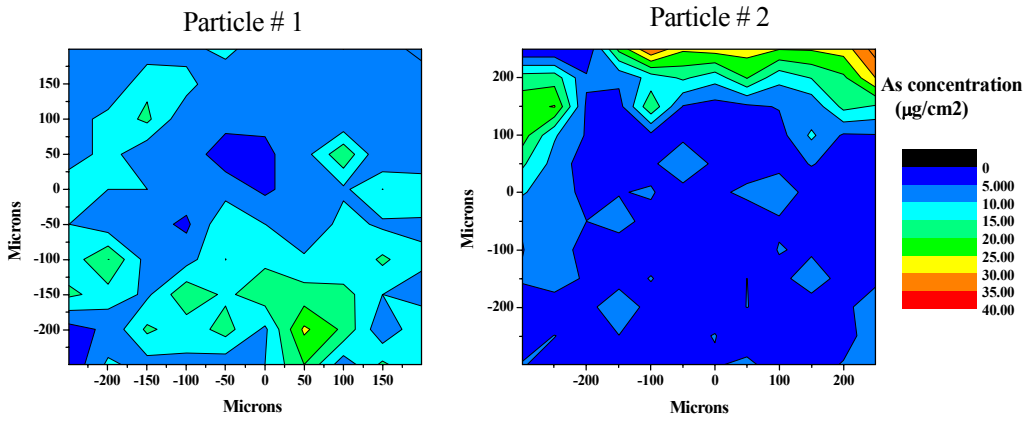

Figure 3. Arsenic concentration map from two different PAC particles.

Ion Scattering Simulations of Misfit Dislocations at the Single Crystal Fe_2O_3/Al_2O_3 Interface

S Maheswaran,[(a)] S Thevuthasan,[(b)] F Gao,[(c)] V Shutthanandan,[(b)] and CM Wang[(b)]

(a) University of Western Sydney, Penrith Campus, Kingswood, Australia

(b) W.R. Wiley Environmental Molecular Sciences Laboratory

(c) Pacific Northwest National Laboratory

Disordering at the buried interface can be investigated using ion scattering techniques such as Rutherford backscattering spectrometry (RBS) and channeling. When single crystal α-Fe_2O_3 thin films are deposited on α-Al_2O_3 (0001) substrates using oxygen plasma assisted molecular beam epitaxy, a periodic distribution of basal dislocations occurs due to lattice mismatch along the interfaces. Such misfit dislocations were investigated using RBS and high resolution transmission electron microscopy (HRTEM) in single crystal α-Fe_2O_3(0001) thin films, which were epitaxially grown on α-Al_2O_3 (0001) substrates (Thevuthesa et al. 2001). HRTEM measurements showed that these dislocations lie at the interface about 7.0 nm apart and the interface peaks seen in ion scattering results are consistent with the HRTEM results (Thevuthesa et al. 2001). Molecular dynamics simulations (MD) were performed to understand the formation of misfit dislocations and the interface structural features (Gao in press).

Figure 1 shows the atomic arrangement of Fe and Al at the interface around two partial misfit dislocations. Ion scattering simulations were carried out using VEGAS code. Atomic positions generated during the MD simulations were used in these simulations and the results were compared with experimental results. The VEGAS code uses Monte Carlo simulations based on the Moliere screened potential to calculate the hitting probabilities. The current VEGAS code can handle only up to 2200 atoms in a cluster. Since the big cluster generated during the MD calculation has a significantly larger number of atoms than the VEGAS code limit, the large cluster was divided into nine small clusters for VEGAS simulations. Figure 2(a) shows displacement of atoms at the interface of an atomic row that

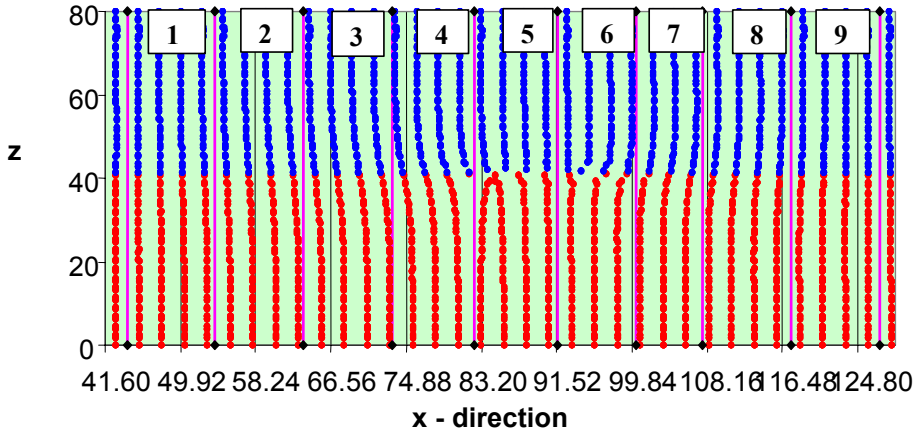

Figure 1. Fe_2O_3/Al_2O_3 interface showing the atomic arrangement of Fe and Al atoms from the MD calculations.

is in the proximity of the misfit dislocations (4th row from the misfit dislocation). Hitting probabilities generated for the atoms in this row using VEGAS code are presented in Figure 2(b). As expected, the hitting probabilities are significantly higher for the surface and interface atoms, which are visible to the ion beam. The average hitting probabilities determined for Fe and Al atoms in the surface and interface regions are compared with the experimental results in Table I. Although the hitting probabilities for Fe in the interface region is different between the experiment and simulations (probably due to defects in the film and incomplete one dimensional MD calculations), there is a good agreement between the experimental and simulated hitting probabilities for Fe in the surface and Al in the interface regions. The combination of MD and VEGAS simulations with RBS and HRTEM measurements shows promising results in understanding the interface structures of this single crystal Fe_2O_3/Al_2O_3. At present, we are working on the full two dimensional MD calculations of this interface.

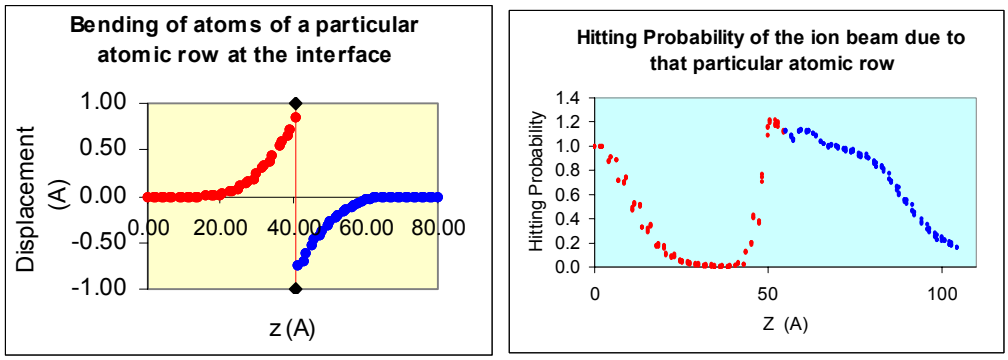

Figure 2. (a) Displacement and (b) hitting probability of Fe and Al atoms of a particular atomic row at the interface.

Table I. Simulated Hitting Probabilities and Experimental Peak Areas

	Fe – Surface Peak (atoms/row)	Fe – Interface Peak (atoms/row)	Al – Interface Peak (atoms/row)
Unrelaxed Dislocation – x dir.	3.9	-	3.5
Unrelaxed Dislocation – y dir.	3.9	-	5.2
Unrelaxed Dislocation – both x & y directions	3.9	-	6.2
Relaxed – MD cal. Dislocation – x dir.	3.7	1.5	8.2
Experiment	3.9	4.3	7.3

References

Gao, F, CM Wang, S Maheswaran, and S Thevuthasan. Atomic Level Simulations of Misfit Dislocations at the Interface of Fe_2O_3/Al_2O_3 System. *Nucl. Inst. And Meth. B*, (in press).

Thevuthasan, S, V Shutthanandan, EM Adams, and S Maheswaran. High Energy Ion Beam Analysis of Buried α–$Fe_2O_3(0001)/\alpha$-$Al_2O_3(0001)$ Interface. *AIP Conference Proceedings*, July 12, 2001, Vol. 576, pp. 432–435.

Direct Observation of Atomic Disordering at the $SrTiO_3$/Si Interface Due to Oxygen Diffusion

V Shutthanandan,[(a)] S Thevuthasan,[(a)] EM Adams,[(b)] Y Liang,[(c)] Z Yu,[(c)] and R Droopad[(c)]

(a) W.R. Wiley Environmental Molecular Sciences Laboratory
(b) Whitman College, Walla Walla, Washington
(c) Physical Sciences Research Laboratories-Motorola Laboratory

Several high dielectric oxides including ZrO_2, Y_2O_3, Ta_2O_5, and (Ba, Sr)TiO_3 were explored as potential candidates to replace conventional SiO_2 as gate oxide materials in semiconductor devices. Although these materials show promising dielectric behaviors, critical issues, such as interfacial electronic and structural properties, still need to be addressed in most cases. Integration of single-crystal oxides with Si represents a new approach to address some of the issues associated with interfaces. Recently, it has been demonstrated that a number of single-crystal perovskite oxides such as $SrTiO_3$ (STO) and $BaTiO_3$ could be successfully grown on Si substrates using a molecular beam epitaxial (MBE) method . Some of these films were tested in device technology and the results showed promising behavior including low leakage current and interfacial density states. However, the interface chemistry and stability need to be addressed, especially at various annealing temperatures and in different environments. We report the direct observation of atomic disordering and growth of amorphous silica at the STO/Si interface due to oxygen diffusion from the film to the interface at elevated temperatures in vacuum and oxygen environments.

The samples were grown by a MBE method and several pure single crystal STO films with thickness ranging from 2 nm to 100 nm were used in this study. Rutherford Backscattering spectrometry (RBS) and nuclear reaction analysis (NRA) measurements were carried out in channeling and random geometries to determine the structural and compositional properties of the film. The total number of ^{16}O and ^{18}O atoms in the films was determined using $^{16}O(d,p1)^{17}O$ and $^{18}O(p,\alpha)^{15}N$ nuclear reactions. The stoichiometry of the film was determined by the RBS to be Sr:Ti:O = 1:1:3. The minimum yields (the ratios of the aligned yield to the random yield just below the surface peaks) for both Sr and Ti are approximately 3%, thus the film appears to be well ordered and comparable to high quality bulk STO single-crystals. Seven distinct peaks were visible in the aligned spectrum, which is presented in Figure 1. The first peak at the high-energy side is the surface peak from Sr atoms at the front of the film (Sr-SP). The second peak is attributed to some Sr atoms visible to the ion beam at the STO/Si interface (Sr-IP). Similarly, the next two peaks are surface (Ti-SP) and interface (Ti-IP) peaks related to Ti

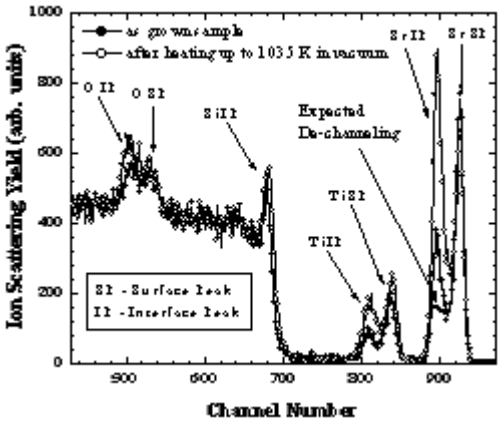

Figure 1. Channeling spectra from as-grown (closed circles) and vacuum annealed (open circles) 40 nm thick STO films on Si are shown.

atoms. Some Si atoms at the interface are also visible to the ion beam, and this is evident from the fifth peak in the spectrum (Si-IP). The sixth peak is related to the backscattered ion contribution due to the surface oxygen atoms (O-SP) from the film and the last peak is due to the visibility of oxygen atoms to the ion beam at the interface (O-IP).

In order to investigate the interfacial structural and chemical behaviors at elevated temperatures, the STO/Si samples were heated in vacuum from 675 K to 1075 K in 100 K steps and subsequently subjected to RBS, NRA, and XPS characterization. Channeling spectra from as-grown film and the film annealed to 1035 K in vacuum are shown in Figure 1. The area of interface peaks related to all three sublattice atoms (Sr, Ti and O) in the film and Si in the substrate are significantly increased after 1035 K vacuum annealing compared to those related to the as-grown sample. The total number of oxygen atoms in the sample (surface and interface regions) before and after this annealing were measured using the $^{16}O(d,p1)^{17}O$ nuclear reaction. It was found that there was no significant difference in the total number of oxygen atoms before and after annealing within the experimental uncertainties. This suggests that the oxygen atoms removed from the film mostly migrated to the interface and resulted in a large increase in the O and Si IP areas during annealing. These results suggest that thermodynamically it is more favorable for the growth of silica than for strontium titanate at these temperatures.

Atomic disordering of all sublattices appears to be gradually increasing as a function of annealing temperature (Figure 2). This clearly indicates that there is a gradual oxygen movement from the film to the interface for the silica growth at the interface as a function of annealing temperature. Similar increases in both Sr and Ti IP areas suggests that the disordering in both sublattices in the interface region is similar in nature. Si and O IP areas appear to be increasing as a function of annealing temperature due to silica growth at the interface. Significant increases in Sr and Ti IP areas compared to their SP areas suggests that there is significantly large disordering in the interface region compared to the surface region. Similar sets of annealing experiments were carried out in oxygen (^{18}O) environment on another sample from the same wafer to understand this observation. The behavior of Si and O IP appears to be similar between vacuum and oxygen annealing, possibly due to the similar order of silica growth in both processes. Although silica growth at the interface is in the same order as the vacuum heating experiments, there was no significant increase in Sr and Ti IP areas as a function of annealing temperature. This clearly suggests that, during the vacuum heating, the structural changes in the interface region were mainly due to the large oxygen removal from the interface region.

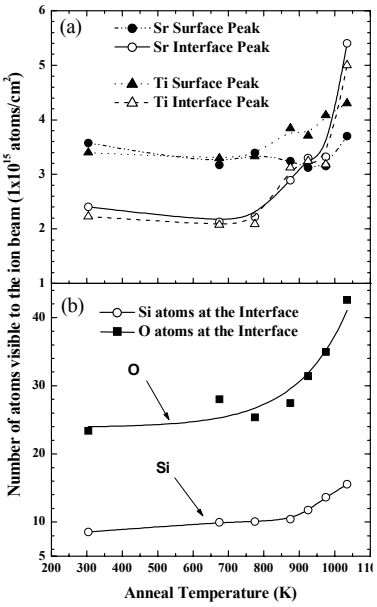

Figure 2. Total number of surface and interface (a) Sr and Ti, and (b) O and Si atoms visible to the incident ion beam as a function of annealing temperature.

XPS and AFM Study on Corrosion Behavior of Rock Bolt Carbon Steel for Yucca Mountain Repository

V Deodeshmukh,[(a)] D Chandra,[(a)] S Lea,[(b)] and M Engelhard[(b)]
(a) University of Nevada, Reno
(b) W.R. Wiley Environmental Molecular Sciences Laboratory

Yucca Mountain (YM) repository for disposal of high-level radioactive wastes requires reinforcements, such as rock bolts, and steel sets for the tunnel (Figure 1). Carbon steels that are widely used as structural materials due to their low cost and uniform corrosion behavior have been proposed as a candidate material for the rock bolts, and steel sets. However, they are also prone to localized corrosion depending on the severity of the environment. Conventional macroscopic corrosion methods give corrosion rates, and insights to the passivation potentials and other related parameters. Understanding of the long-term corrosion behavior at the microscopic and nanoscale levels is vital for these rock bolts that are under significant stress, which is compounded by the prevailing YM repository environment and expected changes in tunnel temperatures during the next hundreds of years.

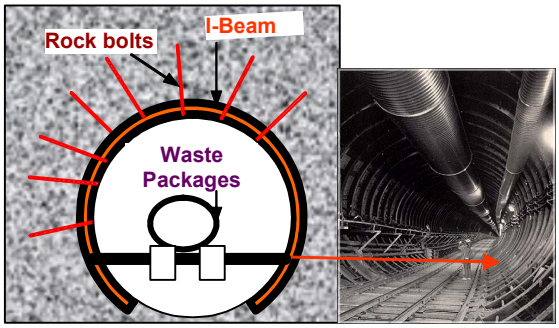

Figure 1. Schematic (left-not to scale) depicting rock bolt and I-beam or steel set placement in the repository tunnel. A photograph of the Nevada YM test tunnel (right-taken from YM website) showing the actual arrangement of the steel sets. The rock bolts (not observable in the photo) experience severe loads in pre-stressed condition and during rock movement. Numerous reinforcing rock bolts will be used in these tunnels for reinforcement purposes.

Electrochemical polarization and impedance methods have been used for a corrosion study that yielded anodic and cathodic behavior of the steels. X-ray Photoelectron Spectroscopy (XPS) gave the compositional changes and elemental oxidation states as a function of depth from the surface. These characterization methods were then used to connect to the macroscopic results. Further, atomic force microscopy (AFM) reveals dynamic behavior under electrochemical polarization. These methods have been used at PNNL to understand the corrosion behavior of the YM steels. In the case of XPS studies, the samples were polarized *ex-situ* and examined in XPS using depth-profiling methods. The changes in temperatures may lead to changes in electrolyte concentration in the repository. Thus, dissolved ion concentration effects of various species were studied. Among these ions, chloride, HCO_3^-, and SiO_3^{2-} ions are important in deciding the performance of carbon steels for the YM repository. Contact mode AFM was conducted at PNNL to study the pit depth and surface morphology of the specimens potentiostatically polarized at passive potentials (Deodeshmukh et al. in press; Castro et al. 1991, Seal et al. 2000).

Electrochemical analyses showed that the combined effect of bicarbonate and silicate ions exhibit better corrosion resistance for the rock bolts. XPS depth profiling results of Fe(2p), O(1s) and C(1s) showed details of chemical composition changes, at nanometer levels, in the

(extrinsic) passive film formed on the rock bolt steel surfaces. Comparing the passive films formed in 3.5% NaCl solution containing 0.5M HCO_3^-, and 0.5M HCO_3^- + 0.01M SiO_3^{2-}, it was found that film thicknesses were approximately 40 and 100 nm, respectively (Figure 2). One of the major phases on the surface was $FeCO_3$, due to the reaction: $Fe^o + HCO_3^- \rightarrow FeCO_3 + H^+ + 2e^-$ at $E^o = -0.735$ V.

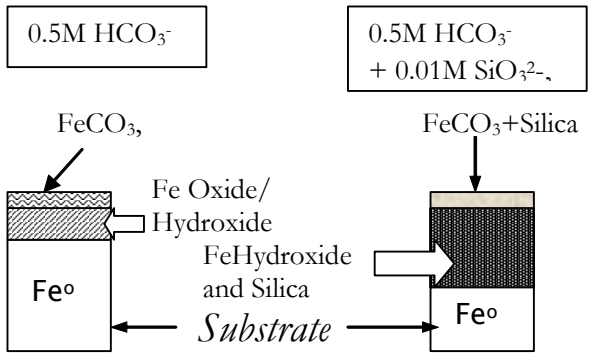

Figure 2. Schematic of the passivated films formed on rock bolt steel surfaces in the presence of 3.5% NaCl with bicarbonate added. XPS measurements indicate the 40nm film formed is primarily a mixed Fe Oxide/Hydroxide with $FeCO_3$ at the outermost surface. When silicate is added, a much thicker passivating film with silica present throughout is evident. The increased passivation can be attributed to the adsorption of silicates to pits or defects in the passive film.

AFM images were also taken with contact mode to study the pit depth and surface morphology of the specimens potentiostatically polarized at passive potentials. AFM images observed for 0.5M HCO_3^-, 0.01M SiO_3^{2-} and in 0.5M HCO_3^- + 0.01M SiO_3^{2-} solutions showed a pit depth of 2.23 μm in bicarbonate solutions, while in silicate the pit depth was about 1.6 μm. Combined bicarbonate and silicate ions showed a much smaller pit depth of 710 nm as compared to individual bicarbonate and silicate ions. Thus films formed due to combined ions were more effective at inhibiting corrosion than those formed by the bicarbonate and silicate ions individually. This effect is due to absorption of silica near the pits, which inhibits further growth of pits.

Combining electrochemical and characterization methods such as XPS/AFM gives a good understanding of the nanoscale corrosion mechanisms. These studies are now being extended to other materials.

References

Deodeshmukh, V, V Arjunan, D Chandra, J Daemen, and DA Jones, A Yilmaz, S Lea and M Engelhard. Effect of Bicarbonate and Silicate Ions on the Passivation Behavior of Carbon Steel in 3.5% NaCl Solution, Manuscript in review, *Corrosion Science* (in press).

Castro, EB, JR Vilche and AJ Arvia. *Corrosion Science*, 32: p.37 (1991)

Seal, S, K Sapre, A Kale, V Desai, M Gopal and P Jepson, *Corrosion Science,* 42, p. 1623 (2000).

This research is sponsored by the US Department of Energy, Yucca Mountain Project Task 18 DE-FC08-98NV12081.

Use of Transmission Electron Microscopy to Investigate Novel Oxide-Supported Hydrotreating Catalysts

ME Bussell,[(a)] CM Wang[(b)]

(a) Western Washington University, Bellingham

(b) W.R. Wiley Environmental Molecular Science Laboratory

Transmission electron microscopy (TEM) has been used to investigate the structure of novel hydrotreating catalysts. These materials, metal phosphides, and bimetallic carbides and nitrides, are being developed for their possible use in a new generation of catalysts to remove sulfur and nitrogen impurities from fossil fuels. The catalysts are synthesized by undergraduate and M.S. level students at Western Washington University (WWU) and are characterized by a variety of techniques at both WWU and the Environmental Molecular Sciences Laboratory of PNNL.

Shown in Figure 1 is a TEM image of a silica-supported nickel phosphide (Ni_2P/SiO_2) catalyst prepared using a synthesis procedure developed in our laboratory. The crystallite size (~18 Å) and lattice spacing are consistent with X-ray diffraction measurements of the catalyst. The hydrodesulfurization (HDS) activities of a series of Ni_2P/SiO_2 catalysts with a wide range of Ni_2P loadings have been evaluated in a flow reactor system using a feed consisting of thiophene (C_4H_4S) in hydrogen. The Ni_2P/SiO_2 catalysts have high HDS activity with a 30 wt% Ni_2P/SiO_2 catalyst nearly 15 and 3.5 times more active than conventional sulfided Mo/SiO_2 and $Ni\text{-}Mo/SiO_2$ (Ni/Mo = 0.5) catalysts.

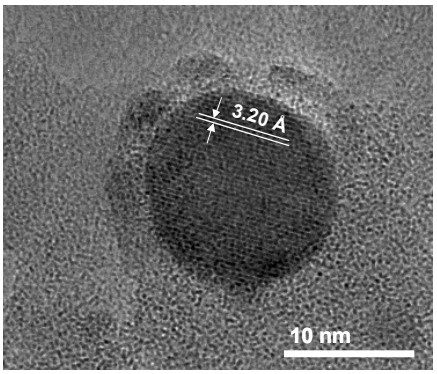

Figure 1. A TEM image of a Ni_2P crystallite at the surface of a 25 wt% Ni_2P/SiO_2 catalyst.

Temperature Induced Phase Separation in Chromium Films

L Sara,[(a)] C Wang,[(a)] MH Engelhard,[(a)] and DR Baer[(b)]
(a) W.R. Wiley Environmental Molecular Sciences Laboratory
(b) Pacific Northwest National Laboratory

Chromium metal is known to change its phase upon size reduction. In this study the possibility of controlled phase separation in chromium has been obtained using the knowledge that nanophase chromium exists in a δ-A15 type structure—apart from a recently observed fcc phase. The δ-A15 structure is stable up to 428–450°C where significant grain growth and phase transformation to the bcc structure occurs. Also, nanophase Cr suppresses non-magnetic antiferromagnetic phase transition and gives rise to a surface ferromagnetic phase. Thus, selective phase transformation or controlled phase separation in chromium can be useful for technological applications due to changed physical properties as a result of different electronic structure with the same base material.

Rapid evaporation and cooling at a close source-to-substrate (SS) distance can be viewed as a method to get phase separation where the effect of temperature gradient during the growth of films caused by the heated source can be used to generate phase separation. Normal vacuum evaporation results in a nanophase rich interfacial region, forms due to interfacial stress followed by mixed grain region (nanophase and bulk). Existence of the mixed grain region leads towards a phase mixture in metals like chromium. Annealing these films above 450°C leads transformation to bcc phase leaving a very thin nanophase interfacial layer due to stress. On the other hand, mixed grain region could be minimized if the temperature from the source could be used to force a phase transformation in the mixed phase/grain region to a single phase during the growth. Thus initial growth conditions would favor the formation of thicker nanophase chromium and later the source heating could enhance formation of the bcc bulk phase.

Vacuum evaporations of chromium on Si (100) were carried out at 3×10^{-5} Pa at SS distance of 2 cm and 32 cm. The evaporation rate was maintained ~ 3 μm/min, the fastest possible in our system. The tungsten filament of the evaporator also served as the heating source. During evaporation, no additional heating was provided to the substrate. *In-situ* thickness measurements were done using a quartz crystal thickness monitor. Films grown at SS distances of 2 cm and 32 cm were 800 nm and 20 nm thick, respectively. The samples were exposed to atmospheric pressure fifteen minutes after closing the filament current to ensure no additional sample heating due to source filament, especially for the short distance depositions.

The films were analyzed using high-resolution cross-section high resolution transmission electron microscopy (HRTEM), atomic force microscopy (AFM), and X-ray diffraction (XRD) measurements. A cross-section TEM of chromium film deposited at a SS distance of 2 cm is shown in Figure 1a as a columnar type structure. HRTEM across the interface of chromium and silicon in the film deposited at a SS distance of 2 cm is shown in Figure 1b.

A 70 Å thick layer of chromium nanograins is observed near the interface with a very sharp interface between Si and SiO_2. Existence of a δ-A15 phase of chromium was verified by a cross-section electron diffraction pattern (inset of Figure 1b). Bright reflection circles corresponding to reflections in α-bcc chromium such as (110), (200), (211) and (220) are clearly visible. Reflections denoted by b, c and d correspond to (200), (210) and (211) of the δ-A15 phase of chromium.

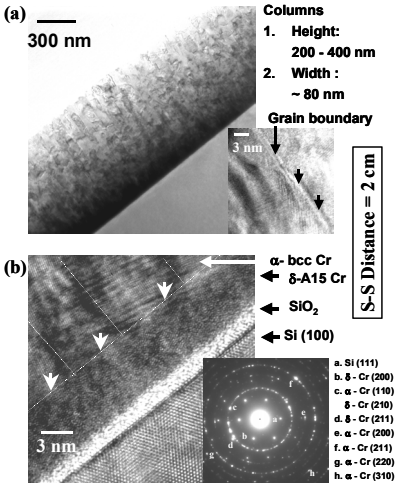

Figure 1. Cross-sectional TEM micrographs of chromium film deposited at SS distance of 2 cm. (a) Low magnification image across the interface. Inset: HRTEM section of the grain boundary region. (b) HRTEM across the interface indicating phase separation. Inset: Electron diffraction.

Columnar growth of chromium with increasing thickness is due to the combination of increased temperature due to radiative heating from the source as well as absence of interfacial stress. Chromium evaporates at 2672°C in atmospheric pressure whereas at 3 X 10^{-5} Pa, evaporation is expected at ~ 072°C. As shown in the schematic of Figure 2, filament is sufficient to act as an electromagnetic radiation source (transfers heat in vacuum), and affects temperature on the substrate surface. This significantly reduces the mixed phase/grain region due to grain growth to bulk α-bcc phase and creates maximum phase separation. As observed in Figure 1a, chromium grains above the initial nanophase growth region are large enough for structural transformation to the α-bcc phase. The factors that impact separation are initial low temperature growth conditions and a later rise in the substrate surface temperature. Surface temperature in the columnar region may well be exceeding 428°C, a temperature required for phase transition to the α-bcc phase.

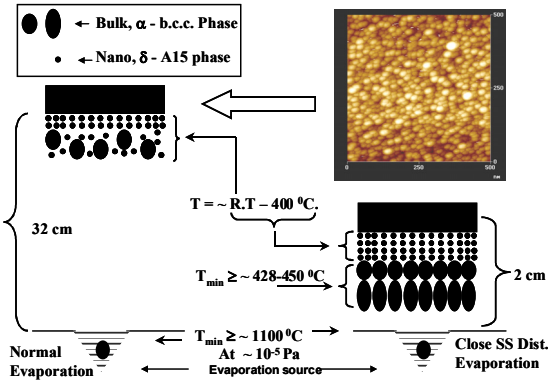

Figure 2. Schematic representation of experimental conditions at SS distances of (a) 2 cm, (b) 32 cm. Top right: surface morphology of chromium film evaporated at a SS distance of 32 cm.

In conclusion, a sharp phase separation between δ-A15 and α-bcc chromium has been obtained using a close distance rapid evaporation where the temperature gradient as well as interfacial stress combined to achieve separation between nanophase chromium and bulk columnar grains. It is known that a large difference exists in magnetic moments of atomic and bulk chromium, which suggests that interesting magnetic effects may occur by inter-atomic distance modulation and/or with phase separation. Observed suppression of antiferromagnetic order and rise in surface magnetization in nanophase chromium can be used to create layered phase separated structures with varying magnetic properties, where a single element system with changed physical properties can be used to replace multi-component systems.

X-Ray Photoelectron Spectroscopic Study of Gold Nanoparticle Catalysts

MM Maye,[(a)] J Luo,[(a)] Y lin, [(b)]MH Engelhard,[(c)] and CJ Zhong[(c)]

(a) State University of New York at Binghamton

(b) Pacific Northwest National Laboratory

(c) W.R. Wiley Environmental Molecular Sciences Laboratory

Nanostructured gold catalysts have attracted increasing interest since the pioneer work of Haruta which demonstrated unusually high catalytic activities for CO oxidation when the nanoparticles were made less than ~10 nm diameter in size and supported on oxides. It is possible to use core-shell gold nanoparticles to construct the catalyst and activate the catalytic activity by applying an anodic polarization potential. Understanding how the core-shell surface components reconstitute in such a catalytic activation process will have important implications in expanding this approach to the design and fabrication of nanostructured catalysts. We report herein the results of a study of decanethiolate-capped gold nanoparticles of 2-nm and 5-nm core sizes assembled on planar substrates using 1,9-nonanedithiol (NDT) and 11-mercaptoundecanoic acid (MUA) as molecular linkers which were studied as a model system. XPS is employed to detect the identity of surface species and to analyze the elemental composition or oxidation states of the nanomaterials, from which we derive structural information about the surface reconstitution of the core-shell nanostructured catalysts.

Figure 1 shows a representative set of XPS spectra for the NDT-$Au_{2\text{-nm}}$ film (Maye et al. 2003). The spectra are shown for the regions of S(2p) (A), O(1s) (B), and Au(4f) (C). The C(1s) feature at 284.6 eV is not included because it is largely from the carbon (HOPG) substrate. The as-prepared film (a) and the electrochemically-activated film (b) are compared in each spectral region. The S(2p) region (Figure 1A) is characterized by a doublet that arises from spin-orbit coupling ($2p_{3/2}$ and $2p_{1/2}$). For most neat thiols, this region is generally defined by the more intense $2p_{3/2}$ band which lies between 163 and 165 eV. In contrast, the binding energy (BE) observed for monolayers derived from thiols in which the sulfur species interact strongly with the surface Au(I) are ~1 eV lower, i.e., ~162 eV for the $2p_{3/2}$ band. The deconvolution of this doublet using $2p_{3/2}$ to $2p_{1/2}$ intensity ratio of ~ 2:1 as a constraint (dashed lines under the S(2p) envelop) reveals a small fraction of doublet component at 163.5 and 164.5 eV, which we believe is likely due to the free -SH group from one end of the NDT linker molecule. This component is more significant in the S(2p) spectra for NDT-$Au_{5\text{-nm}}$ film (not shown). After the catalytic activation, the S(2p) band

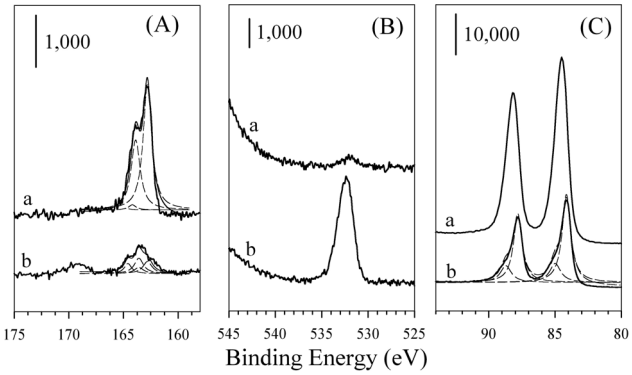

Figure 1. XPS spectra in regions of S(2p) (A), O(1s) (B) and Au(4f) (C) for a NDT-$Au_{2\text{-nm}}$ film before (a) and after (b) the electrochemical activation.

intensity is significantly reduced, but still detectable, indicating a partial removal of the thiolates species. The remaining (S2p) band is due to the presence of unremoved thiolates and a weakly-bound -SH group from one end of NDT. The detection of the small band at 169.2 eV is indicative of the presence of sulfonate species ($-SO_3^-$). The finding implies the possibility that the desorption of the capping/linking agent involves oxidation of thiolate to sulfonate species. The surface relative compositions for both sulfur and oxygen species are changed after the catalytic activation. The net change of sulfur percentage (from 8.2% to 2.1%) corresponds to a 75% removal of the thiolate capping/linking monolayers on the gold nanocrystals by the electrochemical activation. The sulfonate species detected is ~20% of the remaining sulfur-containing species. This mechanism is qualitatively consistent with earlier findings in studies of electrochemical oxidative desorption of self-assembled alkanethiolate monolayers on planar gold surfaces. A similar S(2p) spectral feature is observed for MUA-linked film.

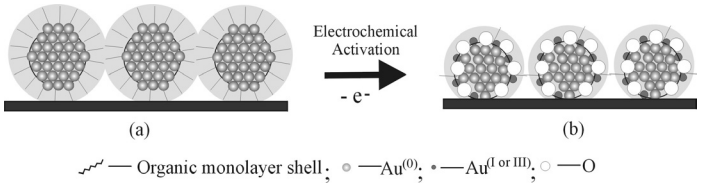

Figure 2. A schematic illustration of the electrochemical activation of the assembled nanoparticles. (a) before activation. (b) after activation.

Two main conclusions have been arrived about the electrochemically activated catalysts: 1) there is a partial opening of the capping/linking nanostructure as a result of the removal of the thiolates; and 2) surface oxides are formed on the gold nanocrystals. The implications of these conclusions are illustrated in Figure 2, where the surface structure of the activated nanocrystals is either partially or completely reconstituted with the relative coverage of the surface oxide species being dependent on the nature of the interparticle capping/linking thiolates. This surface reconstitution model is qualitatively supported by electrochemical quartz crystal nanobalance (EQCN) and atomic force microscopic (AFM) data. We believe that both the nanoscale morphology and the surface oxide have been operative factors in determining the catalytic activity. Quantitatively, which of these two factors is most important remains to be investigated. We are currently studying other activation conditions (e.g., reductive or oxidative activation) to address this issue. In view of the presence of the trace amount of thiolates in the activated thin film of gold nanoparticles, an important question is how it affects the catalytic activity. Recent work using refined electrochemical activation and other catalytic activation routes such as chemical and thermal activation have demonstrated the viability of a complete removal of the thiolates. Research in this direction is in progress to help unravel mechanisms for the nanostructured gold catalysts.

References

Maye, MM, J Luo, Y Lin, MH Engelhard, M Hepel, and CJ Zhong. X-ray photoelectron spectroscopic study of the activation of moleculary-linked gold nonoparticle catalysts. *Langmuir*, **19,** 125-131 (2003).

User Projects

Investigations Of Zro_2 and $Nano_3$ Inferfaces Using HREELM
E Paparazzo
Istituto de Struttura della Materidel CNR, Frascati, Rome

Surface and Interface Studies Of MBE Grown Epi-Oxides on Oxide and Silsubstrates
JY Zhiyi
Motorola

Biotransformation of Iron Minerals
YA Gorby
Pacific Northwest National Laboratory

Purity Analyses of DNA
NG Isem
Pacific Northwest National Laboratory

HREM Work on Unirradiated Inconel 718
BH Sencer
Pacific Northwest National Laboratory

X-Ray Photelectron Spectroscopy Studies of Multicomponent Self Assembling Monolayers on Gold
BJ Tarasevich
Pacific Northwest National Laboratory

TPD Study of $SrTiO_3$
L-Q Wang
Pacific Northwest National Laboratory

Environmental Degradation Mechanisms in Lightweight Transportation Alloys
CF Windisch
Pacific Northwest National Laboratory

Growth of Magnetic Metal Oxide Thin Films
U Diebold
Tulane University, New Orleans, Louisiana

Correlation Between Bulk and Surface Defects in Rutile TiO_2
U Diebold
Tulane University, New Orleans, Louisiana

Energetic Processes: Reaction in Thin Organic Films
GB Ellison
University of Colorado, Boulder

Barium Ferrite Thin Film/Particles for Magnetic Recording and Microwave Applications
KH Yang
University of Idaho, Moscow

Theoretical Studies of Kinetic Processes in Nanoscale Ice Films
H Jonsson
University of Washington, Seattle

Environmentally Induced Changes in Structure of Fruit Cuticle
EA Curry
USDA/ARS Tree Fruit

SEM Studies of Laser-Ablated Material
JT Dickinson
Washington State University, Pullman

Nanocoating
J Liu
Pacific Northwest National Laboratory

Growth and Structure of Epitaxial Pure and Zr-Doped CeO_2 by Oxygen-Plasma Assisted Molecular Beam Epitaxy
YJ J Kim
Taejon National University of Technology, South Korea

Rutherford Backscattering and Channeling Studies of Ceria and Iron Oxidethin Films
S Maheswaran
University of Western Sydney, Nepean, Australia

Use of Phillips XRD in EMSL 1422
SC Smith
Pacific Northwest National Laboratory

Investigation of PbGe Thin Films
T Li
Sharp Microelectronics Technology, Inc.

Crystalline and Amorphous Phase Study Of Peralkalin
LL Davis
Pacific Northwest National Laboratory

Xray Photoelectron Diffraction of Mgo(111)-(1x1)
M Gajdardziska-Jo
University of Wisconsin, Milwaukee

Formation and Composition of Biogenic Iron Minerals
YA Gorby
Pacific Northwest National Laboratory

MOCVD Growth of Cap Films
H Lu
University of Washington, Seattle

Hydrocarbon Contaminants to Degradation by Soil Microorganisms Alkylati on Experiments Using CRTS
MR Phelps
Pacific Northwest National Laboratory

New Silicotitanate Waste Forms: Development and Characterization
YJ Su, L Li
Pacific Northwest National Laboratory
H Xu
University of California Davis

Catalyst Synthesis
Y Wang
Pacific Northwest National Laboratory

Plasma Modification of Antifouling Separation Membrane Surfaces
L Liang
Pacific Northwest National Laboratory

Application of Tunable, Ultrafast Lasers to Ion-Trap Mass Spectrometry
RF Haglund Jr., DR Ermer, M Papantonakis
Vanderbilt University, Nashville, Tennessee

Non-Stoichiometric Precipitation of Phase-Pure Hydrotalcite-Like Compound
RK Kukkadapu, JE Amonette
Pacific Northwest National Laboratory

Development of Advanced Durable Lean NOx Catalysts for Diesel Engine Aftertreatment
PW Park, K Koshkarian
Caterpillar, Inc.

Investigations of Organic Light Emitting Diode Materials
AL Johnson, LS Sapochak
University of Nevada Las Vegas

Tapping Mode AFM for Real-Time Analysis of DNA Hybridization on Microarrays
EM Jutras
Pacific Northwest National Laboratory
DR Call
Washington State University, Pullman

Mapping of the Contaminants in Soil Thin Sections
OG Povetko
Oregon State University, Corvallis

Plasma Coating for Surface Passivation of Silica-Coated Wafers
S Baskaran
Pacific Northwest National Laboratory

Hydrophobic Coatings Development for Contactor Membranes
DW Matson
Pacific Northwest National Laboratory

Surface Structure Analysis of Hematite Thin Films Grown by MBE Technique
LD Marks, PC Stair, N Erdman, L Cheng
Northwestern University, Chicago, Illinois

DNA Microarray Automation and Analysis
J Nelson, DW Weaver
Pacific Northwest National Laboratory
DR Call
Washington State University, Pullman
DP Chandler
Argonne National Laboratory

Evaluation of SIMS to Measure N Isotopes in Soils
JB Cliff
Oregon State University, Corvallis

Deposition of Low-Temperature ITO on Flexible Polymer Substrates
PM Martin
Pacific Northwest National Laboratory

Chemical Imaging of Quantum Dots
H Luo
New York State University of Buffalo

Coal Surface Charging Property Characterization
MK Mazumder, D Kumar, S Trigwell
University of Arkansas, Little Rock

Analysis of Gases Produced During Plasma Treatment of Surfaces Contaminated with Chemical and Biological Agent Simulants
TM Moeller, M Fountain, L Allen
Innovateck, Inc.

Automated Analysis of Field-Collected Aerosols
JP Cowin, A Laskin
Pacific Northwest National Laboratory

Ion Trap Mass Spectrometry for Planetary Surface Instruments
G Cardell, ME Taylor
Jet Propulsion Laboratory

Studies of Protein Adsorption and Calcium Phosphate Nucleation onto Self-Assembled Surfaces
BJ Tarasevich, R Rajagopal
Pacific Northwest National Laboratory

Surface Films on Molybdenum
JP Cowin
Pacific Northwest National Laboratory

Heavy Ion Damage in Stainless Steel Alloys
BW Arey, SM Bruemmer
Pacific Northwest National Laboratory

Measurements of Hydrogen Absorption in Oxidized Ti Using Nuclear React
R Smith
Pacific Northwest National Laboratory

Catalyst Characterization Using the RXM-100 Test Stand
CL Aardahl, K Rappe, CF Habeger
Pacific Northwest National Laboratory

XRD Analysis of Inorganic Chemicals
LL Reed, S Baum
Battelle Columbus

XPS Analysis of Irradiated Soot Samples
RS Disselkamp
Pacific Northwest National Laboratory

Spin Polarized Studies of Iron Oxide Films
JG Tobin
Lawrence Livermore National Laboratory
D Waddill, S Morton
Lawrence Berkeley National Laboratory

The Growth and Characterization of $Ce_{1-X}Zr_xO_2$ Films
YJ J Kim
Taejon National University of Technology, South Korea

Deposition and Characterization of High-K Dielectric Thin Films
MH Yoon
University of Washington, Seattle
JW (Bill) Rogers
Pacific Northwest National Laboratory

Deposition of High-K Dielectric Thin Films
AC Tuan
University of Washington, Seattle

Ceria-Zirconia Thin-Film Crystals for Electron Microscopy Studies of Metal-Support Interactions in Model Automotive-Exhaust Catalysts
GW Graham
Ford Motor Company

Preparation of Ultra Low Dielectric Constant Silica Films
S Baskaran, X Li, JC Birnbaum, J Liu, CA Coyle
Pacific Northwest National Laboratory

SEM/EDS of Thin Films
CF Windisch, GJ Exarhos
Pacific Northwest National Laboratory

Biogenic Iron Materials
YA Gorby, A Dohnalkova
Pacific Northwest National Laboratory

Interface Chemistry and Electronics of ZnSe and ZnS upon $CuLn_2Se_3$
PA Eschbach
Washington State University, Pullman

Interaction of Water and Formic Acid with Oxide Surfaces
L-Q Wang
Pacific Northwest National Laboratory

Near-Surface Analysis of Geologic Media for Implications of Carbon Sequestration
BM Sass
Battelle Columbus

Texture Analysis of a Ti-6Al-4V Forged Alloy after Different Heat Treatment Conditions
ON Senkov, FH (Sam) H Froes
University of Idaho, Moscow

Gratings Calibration and Characterization
DW Matson
Pacific Northwest National Laboratory

Growth and Characterization of Anatase Films
U Diebold, W Hebenstreit, N Ruzycki
Tulane University, New Orleans, Louisiana

Studies on Drug Release from Biodegradable Hydrogels
BM Jeong, A Gutowska
Pacific Northwest National Laboratory

Hydrophobic Surfaces for Gas/Liquid Separators
VS Stenkamp, W Tegrotenhuis
Pacific Northwest National Laboratory

Surface Structural Determination of $SrTiO_3$(100) Surface Using AR-MSRI
L-Q Wang
Pacific Northwest National Laboratory

Crystal Perfection in Cadmium Zinc Telluride Radiation Detectors
M Bliss
Pacific Northwest National Laboratory

Examination of Failed Capscrew, Metallic Debris, Element Identification
JR LaSalle
Energy Northwest

Lithium Aluminate Characterization
LM Bagaasen
Pacific Northwest National Laboratory

Storage Performance of Carbon Nanotubes
X Gong
Pacific Northwest National Laboratory

Materials for Automotive Sensor Development
GW Coffey
Pacific Northwest National Laboratory

Denox Reactions on Ceria and Zirconia-Modified Ceria
JA Rodriguez, J Hrbek, G Liu
Brookhaven National Laboratory

Chemistry of Cadmium Zinc Telluride Surfaces after Processing
AA Rouse
eV Products

Mev He Ion Implantation in Si Wafers
FS Ohuchi
University of Washington, Seattle

Gold Implantation and Subsequent Formation of Gold Nano-Clusters on Glasamples
SK Sundaram
Pacific Northwest National Laboratory

TGA of Ceramic Powder and Pressed Pellet
DM Paxton
Pacific Northwest National Laboratory

Surface Analysis of Microchannel Surface
Y Wang
Pacific Northwest National Laboratory

Thin Film X-Ray Diffraction Studies of Calcium Phosphate Films
BJ Tarasevich
Pacific Northwest National Laboratory

Field Emission Microscopy of Calcium Phosphate Films
BJ Tarasevich
Pacific Northwest National Laboratory

Immobilization of Radionuclides in the Hanford Vadose Zone by Incorporation in Solid Phase
NP Qafoku
Pacific Northwest National Laboratory

In-Situ Experiments in Environmental Scanning Electron Microscope (ESE)
VY Guertsman
Pacific Northwest National Laboratory

XRD Data Analysis and Consultation
ME Bussell
Western Washington University, Bellingham

Chemistry of Mesoporous Silica Films
S Baskaran, GC Dunham
Pacific Northwest National Laboratory

Characterizations of Sol-Gel Derived Mesoporous Silica or Alumina Catalyst for Microchannel Reactor Applications
Y-H (Cathy) Chin
Pacific Northwest National Laboratory

Fixation Mechanisms and Desorption Rates of Sorbed Cs in High Level Waste Contaminated Subsurface Sediments: Implications to Future Behaviour and In-Ground Stability
CC Ainsworth, OS Qafoku
Pacific Northwest National Laboratory

Synthesis, Characterization, and Evaluation of Molybdenum Phosphide Hydrodesulfurization Catalysts
DC Phillips, DH Shorten, ME Bussell, SJ Sawhill, J King, AW Burns
Western Washington University, Bellingham
CHF Peden
Pacific Northwest National Laboratory

Temperature Programmed Reaction of Nitrogen Dioxide Catylysts
CF Habeger
Pacific Northwest National Laboratory

XPS and TOF SIMS Characterization of Surface and Bulk Laser Damage on NIF Optics
AJ Nelson, TW van Buuren, CL Evans
Lawrence Livermore National Laboratory

Deposition and Characterization of Thin Films for Polarized UV Light Emissions
AC Tuan
University of Washington, Seattle

XRD Analysis of Cr(VI) Products From Waste Sites
EC Thornton, JE Amonette
Pacific Northwest National Laboratory

Characterization of Methanol Fuel Cell Components
LJ Ohlsen, AM Chan, GM Rice
Neah Power Systems

XPS Studies of Nickel Cobalt Oxide Films
CF Windisch
Pacific Northwest National Laboratory

The Interaction of Clays with Iron Metal
BA Balko
Lewis and Clark College, Portland, Oregon
JE Amonette
Pacific Northwest National Laboratory

SEM of Aluminum Alloy Sample
VY Guertsman
Pacific Northwest National Laboratory

Investigations of Microbial Spore Lysis Using Near-IR Laser Irradiation
DS Wunschel
Pacific Northwest National Laboratory

Microelectrode Array
JL House, AJ Huffstutter
Oregon Health Sciences University, includes Dept. Oregon Graduate Institute, Portland, Oregon

X-Ray Photoelectron Spectroscopic Study of Chemical Bonding and Electrstructures of the Al_2SIO_5 Polymorphs
FS Ohuchi, S Ghose
University of Washington, Seattle

Low Angle X-Ray Characterization of Catalyst Porosity
CF Habeger, M Delgado, X Li
Pacific Northwest National Laboratory

Preparation of a Langmuir-Blodgett Film of Lipopolysaccharide
BD Wood
Oregon State University, Corvallis
BJ Tarasevich
Pacific Northwest National Laboratory

Study of Manganese Dioxide Reduction during the Transformation of Organic Pollutants
BA Smith, RJ Watts
Washington State University, Pullman

XPS Characterization of Ion-Beam Induced Surface Modification
J Laskin, AK Shukla, E Denisov
Pacific Northwest National Laboratory

Fundamental Studies of Implantation Defects in 4H-SiC
Y Zhang
Uppsala Universitat, Sweden

Development of Chemical Processes for the Mass Production of Carbon Nanotubes
LA Burchfield
Fluor Hanford

The Characterization of the Solid State Materials with Planar Carbon Cluster
H-F Zhang
Washington State University, Pullman

Interfacial Characterization of Self-Assembled Nanoparticle (SNAP) Film Deposited on Al and AA2024
MS Donley
University of Dayton, Ohio
JA Johnson
Wright Patterson AFB/Nichols Research Corporation

Irradiation Effects in Pyrochlore Ceramics
BD Begg
Australian Nuclear Science &Technology Org. (ANSTO)

SEM Imaging of Microstructures
LE Bowman, GC Dunham
Pacific Northwest National Laboratory

SEM of Polyaniline/Fe-Hexacyanoferrate Composite Film
Y Lin
Pacific Northwest National Laboratory

SEM Study of Gold Implanted Gallium Nitride
W Jiang, WJ Weber
Pacific Northwest National Laboratory

Growth and Investigation of Co-Doped Anatase Films
U Diebold, B Katsiev, N Ruzycki
Tulane University, New Orleans, Louisiana

Bromine Etch Rates of P Type Solar Cell Absorbers and SEM, SEM Edax Stuon the Etched Material
PA Eschbach
Washington State University, Pullman
Determination of Metal Dispersion Values
DL King
Pacific Northwest National Laboratory

Measurement of Carbon Cluster Emission from Graphite Sputtered by Noble Ions Near Threshold
RE Stevens
Whitworth College, Spokane, Washington

Fabrication of MIP Filaments
JJ Brazier
Portland State University, Oregon

The Measurement of Low Energy Ion Sputtering Yields Utilizing RBS
MA Mantenieks
Glenn Research Center/NASA

In-Situ High Temperature Oxidation Studies of FeCrAlY Metal
BR Johnson, CL Aardahl
Pacific Northwest National Laboratory

Single-Molecule Imaging At LB Bilayers
HP Lu, GS Harms
Pacific Northwest National Laboratory

Infrared Analysis of Nafion 424 Membrane for Carboxylate Presence
N Nelson
CerOx Corporation
G Spanner
Pacific Northwest National Laboratory

X-Ray Photoemission Spectroscopy of Sulfur-Gold Bond Formation in Monomand Polymer Derived Self-Assembled Monolayers
AL Vance, TW van Buuren, TM Willey, AJ Nelson
Lawrence Livermore National Laboratory

Accumulation of Chromium in *Shewanella oneidensis* MR-1
S Viamajala
Washington State University, Pullman

Influence of Calcium Carbonate Coatings on Contaminant Reactivity
TC Droubay
Pacific Northwest National Laboratory

Polymer Attachment to Glass Vials For Medical Applications
J McGuire
Oregon State University, Corvallis
Chrome Valance State Analysis
MJ Schweiger, O Stahlavsky, TJ Plaisted
Pacific Northwest National Laboratory

Delphi Lithium Battery-2001
GW Coffey
Pacific Northwest National Laboratory

Strengthening Mechanisms in Ultra High Strength Corrosion Resistant Steel
WE Woodm, G Nightingale, G Mares, J Keegan
Portland State University, Oregon

Supercritical Fluid Immersion Deposition of Metal Films on Semiconductor
X-R Ye
University of Idaho, Moscow

Analysis of Silicon Nitride Thin Films
RG Rodriguez
Idaho State University, Moscow

G-Plus Windshield Coating Study
DW Matson
Pacific Northwest National Laboratory

Medicine Container Diagnosis
YB Peng
XL Science & Technology

Sample Production for Neutron Scattering Studies of Co-Doped TiO_2
DV Baxter, D Hussey, M Snow
Indiana University - Bloomington

Design Fabrication and Testing of Series Connected Micro-Electrochemical Sensors
R Radhakrishnan, AV Virkar
University of Utah, Salt Lake City
SC Singhal
Pacific Northwest National Laboratory

Cu Interconnect Structure in the FESEM
DP Field, Y Kusama
Washington State University, Pullman

Photolithography to Form Microcontact Printing Tools
BJ Tarasevich
Pacific Northwest National Laboratory

AES Study of Chemical Segregation in the Ti-Pt-PZT System for Mems Devices
DF Bahr, LR Eakins
Washington State University, Pullman

Film Characterization of Silicon- and Zirconium-Based Sol-Gel Coatings by Scanning Probe Microscopy
N Voevodin, MS Donley
University of Dayton, Ohio
V Balbyshev
Universal Technology Corporation

Creation and Healing of Surface Defects
BD Palmer, Y Liu, RA Mellinger, JD Dudley, EH Wingfield, KI Buxton, DJ Clark, MS Grandy, BM Wolfe, CJ Hohimer, RS Majetich
Hanford High School, Richland, Washington

Determining Mechanism of Pu(VI) Reduction by Manganese Oxides
CJ (Kirk) Cantrell
Pacific Northwest National Laboratory

Electrochemical Storage of Hydrogen in Modified Carbon Nanotubes
L Li
Pacific Northwest National Laboratory

Development of Novel Mass Spectrometry Instrumentation for Real-Time Monitoring of Trace Levels of Volatile Organic Compounds in Air
PT Palmer, W Funk
San Francisco State University, California

Determination of the Factors Controlling Colloid Generation from Altered Waste Forms: TEM Study of Colloid Interactions and Fractal Structure
EC Buck
Pacific Northwest National Laboratory

Accuate Size Measurement of Bacterium SAR-11
SJ Giovannoni
Oregon State University, Corvallis

Microstructure Characterization of Pt on Si
BR Johnson
Pacific Northwest National Laboratory

Polymer Characterization
LS Sapochak
University of Nevada Las Vegas
DW Matson
Pacific Northwest National Laboratory
New Metal Niobate and Silicotitanate Ion Exchangers: Development and Characterization
L Li, YJ Su
Pacific Northwest National Laboratory

Stable Isotopes to Study Nutrient Cycling in Soils
JB Cliff, DD Myrold, PJ Bottomley
Oregon State University, Corvallis
DJ Gaspar
Pacific Northwest National Laboratory

Sea Urchin Biomineralization: A Secondary Ion Mass Spectroscopy (SIMS) Analysis
JM Seto, FH Wilt, G Vrdoljak
Lawrence Berkeley National Laboratory

The Surface Chemistry of Iron Metal in Environmental Remediation Applications
PG Tratnyek
Oregon Health Sciences University, includes Dept. Oregon Graduate Institute, Portland, Oregon

TEM Study of Strontium Bismuth Niobate Ferroelectric Ceramics Doped With Vanadium and Tungsten Oxides
G Cao, SJ Limmer
University of Washington, Seattle

Evaluation of Multicomponent Porous Oxide Films
X Li
Pacific Northwest National Laboratory

Characterization of Aluminosilicate Phases Forming Under Low-Silica Condition
SV Mattigod
Pacific Northwest National Laboratory

Synthesis, Characterization and Testing of Novel Materials for Plasma-Catalyst Technology
CS Lee, SH Noh, HJ Lee, HH Choi, SS Kim, HR Kim
Keimyung University, South Korea

Application of Ion Trap Mass Spectrometry for Analysis of Diesel Exhaust Emissions
MR Smith
Pacific Northwest National Laboratory

Spectroscopy and Microscopy of Doped TiO_2 Nanocrystalline Materials
DR Gamelin, JD Bryan, P Radovanovic, NS Norberg
University of Washington, Seattle

Fuel Reforming Catalyst Characterization
PM Irving, Q (Qimin) Ming
Innovateck, Inc.

Determination of Valance Band Offset in $Sr_2TiO_4/SrTiO_3$ Heterostructures
JH Haen, DG Schlom
Pennsylvania State University, State College

Investigation of Oxidation State of Elements in Natural Brannerites
EC Buck
Pacific Northwest National Laboratory
MX Colella
Australian Nuclear Science &Technology Org. (ANSTO)

Fundamental Studies of Monolayer-Protected Nanoparticles by Gas Chromatography
RE Synovec, GM Gross
University of Washington, Seattle

Epitaxial Growth and Properties of Nanoscale Oxides for Spintronics
D Schmidt, FS Ohuchi, M Olmstead
University of Washington, Seattle

Advanced Actuator Materials Based on Carbon Nanotube Composites
LS Fifield, LR Dalton
University of Washington, Seattle

Interfacing Chip-Based Nanofluidic Systems to Surface-Desorption Mass Spectrometry
JS Kuo, G Fiorini, DT Chiu
University of Washington, Seattle

White Layer Characterization
WE Wood, J Keegan
Portland State University, Oregon

Dilute Magnetic Semiconducting Oxide Thin Films and Nanostructures
KM Krishnan, P Blomquist, A Pakhomov
University of Washington, Seattle

Characterization of Sn Whiskers
MG Norton, J LeBret
Washington State University, Pullman

Growth of MOCVD ZnO on CIGSS Solar Cells
SKN Kundu
Washington State University, Pullman
Texture Studies of Aluminum Extrusion
VY Guertsman
Pacific Northwest National Laboratory

SIMS Analysis of Nickel-Silicon Multilayers
DC Johnson, J Jensen
University of Oregon, Eugene

How Desert Varnish Forms
RS Perry, JT Staley, RS Sletten
University of Washington, Seattle
V Kolb
University of Wisconsin-Parkside

Mev Ion Irradiation of Non-Ice Solar System Analogue Materials
CA Hibbitts, TB McCord, GB Hansen
University of Washington, Seattle

Characterization of Nanocomposites Using Electrochemistry, XPS, TEM and SEM
X-R Ye
University of Idaho, Moscow

Investigating Electrochemical Properties, Composition and Oxidation Statnanoparticles and Catalysts Using Electrochemistry and XPS
C-J Zhong
State University of New York at Binghamton

Exchange Bias in Fe/MnPd Bilayers
GP Blomqvist
University of Washington, Seattle

Development of a Capability to Quantify Arsenic in an Adsorbent
S Maheswaran
University of Western Sydney, Nepean, Australia

Automated Suspension Microarray for Microbial Community Profiling
DP Chandler
Argonne National Laboratory
AE Jarrell
Pacific Northwest National Laboratory

Growth and Characterization of Fe Doped TiO_2 Films
YJJ Kim
Taejon National University of Technology, South Korea

X-Ray Diffraction and Transmission Electron Microscopy Measurements of cobalt Nanospheres, Disks, and Rods
M Beerman
University of Washington, Seattle

Coupling Sequential Flow Prep with PCR and Microarray Detection for Salmpathogens
DR Call, F Loge, D White
Washington State University, Pullman

Determination of Size Distribution of Thermal Spray Powders and the Tungsten Carbide Particle Size and Distribution Present in These Powders
GA Tewksbury
Oregon Health Sciences University, includes Dept. Oregon Graduate Institute
DG Atteridge
Columbia Basin College, Pasco, Washington

Surface Analysis of Polyurethanes
JE Ramsdell
University of Central Florida, Orlando
FA Stevie
North Carolina State University, Raleigh

A Combinatorial Sputtering Approach to Properties Modification in Polaroconducting Films
RR Owings, PH Holloway
University of Florida, Gainesville

Microstructural and Microchemical Analysis of Chalcogenide Nanowires
BR Johnson
Pacific Northwest National Laboratory

Trace Measurements of Organics Due to Pyrolysis of Jet Engine Turbine O
CE Bick, VG Johnston, J Ray
Boeing
ML Alexander, BT Jobson
Pacific Northwest National Laboratory

Mixed Alkali Effect on Oxidation of Si_3N_4 - A Compositional Study Using
HH Du
Stevens Institute of Technology, Hoboken, New Jersey

Preparing Specimens for The Scanning Electron Microscope
JB von Reis, AL Matthiessen, CL Bilskis, J Favela, RE Fox, JE Frazier, A Huffman, S Lyubinetsky, LA Pienaar
Columbia Basin College

Reactivity of Primary Soil Minerals and Secondary Precipitates Beneath Leaking Hanford Waste Tanks
W Um
Pacific Northwest National Laboratory

Use of EMSL Scanning Microscopy Capabilities to Study Soil Mineral Weathering
JT Dickinson, CK Keller, Z Balogh
Washington State University, Pullman

SEM Of Life Stages of Gall Wasps of the Family Cynipidae
JD DeMartini
Humboldt State University, Arcata, California

AFM and XPS Corrosion Research on Rock Bolt for Yucca Mountain Repository
D Chandra, V Deodeshmukh
University of Nevada, Reno

Size Resolved Chemical Composition of Automobile Generated Aerosol Via Single Particle Real-Time Ion-Trap Mass-Spectrometry
DG Imre, A Zelenyuk
Brookhaven National Laboratory

Evaluation of Cold Cap Reaction Layer in a High-Level Waste Melter for DOE-tank Wastes
J Matyas
Pacific Northwest National Laboratory

Chemical State Image Analysis of Biologically Relevant Patterned Surface
B Wickes, DG Castner
University of Washington, Seattle

Magnetics Nanoparticles Characterization
Y Bao
University of Washington, Seattle

XPS Characterization of Hydroquinone-Treated Hematite
CM Eggleston, AG Stack
University of Wyoming, Laramie

Long Term Monitoring of Permeable Reactive Barriers
W Kamolpornwijit
Oak Ridge National Laboratory

Characterization of Advanced Materials: A Summer 2002 Research Experience for Undergraduates
AH Backstrom, DF Bahr, MG Norton, AD LaLonde, PR Leroueil, BD Matson, A-M Cumberlidge, HH Doodnauth, SA Bernard, MA Turner, CC Harris, SC Pevovar, BS McDonald, KL Calvert, ST Lovald
Washington State University, Pullman

Morphology of Colloids Formed in Soils Reacted with Simulated Hanford Waste Tank Solutions and the Distribution of Incorporated and Adsorbed Cesium in the Colloids
Y Deng, JB Harsh, M Flury
Washington State University, Pullman

Reaction Specificity of Nanoparticles in Solution
RL Penn
University of Minnesota, Twin Cities
DR Baer
Pacific Northwest National Laboratory
PG Tratnyek
Oregon Health Sciences University, includes Dept. Oregon Graduate Institute, Portland, Oregon

Cooperation on Nanocomposite Materials Using PNNL/EMSL User Facilities
K Jiang, R Siegel, LS Schadler
Rensselaer Polytechnic Institute, Troy, New York

ESEM Evaluation of MIC in Steel Fittings
BJ Little
Stennis Space Center

Hematite Thin Film Preparation for X-Ray Spectroscopic Studies of The Reactivity and Distribution of Pb(II) and As(V) at Natural Organic Matter/Iron Oxide Interfaces
TH Yoon, GE Brown
Stanford University, California

TEM Use for Analysis of Base Glasses and Doped Glasses
LA Rogers
Pacific Northwest National Laboratory

Assessment of TRI Chemical Emisson Factors from Munitions by Real-Timmass Spectrometric Air Monitoring
CW Spicer
Battelle Columbus Memorial Institute
BT Jobson, ML Alexander
Pacific Northwest National Laboratory

Texture, Morphology, and Stress in PZT Thin Films
DF Bahr, AL Olso, MS Kennedy, LR Eakins
Washington State University, Pullman

Pixel Offset Voltage on a CMOS Liquid Crystal on Silicon Microdisplay
MB Cagle, C Moyer, PA Smith
Three Five Systems, Inc.

Confirmation of Si-C Bonds in Grafted Monolayer through XPS
CD Struckman
South Dakota School of Mines and Technology, Rapid City

Plasma Mechanisms for the Deactivation of Bacterial Spores
JG Birmingham
MicroEnergy Technologies Inc.

Experimental Measurements of the Band Offsets of Epitaxial Silicon on $LaAlO_3$ Single Crystals
LF Edge, DG Schlom
Pennsylvania State University, State College
NA Borjarcz, S Guha
IBM Thomas J. Watson Research Center
SA Chambers
Pacific Northwest National Laboratory

Structural Characterizations of Biogenic Germanium Oxide Nanospheres
C-H Chang, G Rorrer, S-H Liu
Oregon State University, Corvallis
DW Matson
Pacific Northwest National Laboratory

GLAD Coating Microstructure
D Matson
Pacific Northwest National Laboratory

Determination of the Bonding of Various Surfactants onto ZrW_2O_8
ED Swanson
South Dakota School of Mines and Technology, Rapid City

Using Ni-Ion Irradiation for the Development of Advanced Materials for the Next Generation Nuclear Reactor
J Gan, TR Allen
Argonne National Laboratory –West

Characterization of Defects in Nd:YAG Using High Resolution Transmission Electron Microscopy
DE Eakins, G Norton
Washington State University, Pullman

Hydrolytic Stability and Susceptibility of Transition Metal Diolate Complex and Applications to Green Oxidation
KP Gable
Oregon State University, Corvallis

Epoxy-Zirconate Sol-Gel Studies
LS Kasten, MS Donley
University of Dayton, Ohio

Flux Measurements of Biogenic Volatile Organic Compounds by Disjunct Eddy Sampling and Ion Trap Mass Spectrometry Analysis
JV Ortega
University of Colorado, Boulder

A Theoretical and Experimental Investigation of Multiple Splitting for Cr Spectra Generated by X-Ray Photoelectron Spectroscopy
ES Ilton
Pacific Northwest National Laboratory

Molecular Beam Epitaxy Growth of Barium Strotium Titanate
TC Kaspar
University of Washington, Seattle
JW Rogers
Pacific Northwest National Laboratory

XPS Analysis of Oxidized Metal Surface
BR Johnson, Y-H (Cathy) Chin
Pacific Northwest National Laboratory

Studies of the Effect of Particle Size on LA/ICP/MS of Heterogeneous Samples
BW Smith, JDR Gutierrez, JD Winefordner
University of Florida, Gainesville

Characterization of Mn Oxidation State with Electron Energy Loss Spectroscopy
EC Buck
Pacific Northwest National Laboratory

Oxidation Studies of Coatings for Interconnect Plates in Solid Oxide Fuel Cell
RJ Smith
Montana State University, Bozeman

High Resolution Matrix Assisted Laser Desorption/Ionization Imaging of Biological Samples
DS Wunschel
Pacific Northwest National Laboratory

Staff

S. Thevuthasan, Senior Research Scientist – Technical Lead
(509) 376-1375, Theva@pnl.gov

Kyle D. Barker, Student
(509) 376-2708, Kyle.Barker@pnl.gov

Mark H. Engelhard, Science & Engineering Associate
(509) 376-1664, Mark.Engelhard@pnl.gov

Daniel J. Gaspar, Senior Research Scientist
(509) 376-2413, Daniel.Gaspar@pnl.gov

Alan S. Lea, Senior Research Scientist
(509) 376-9145, Scott.Lea@pnl.gov

David E. McCready, Science & Engineering Associate
(509) 376-9648, David.McCready@pnl.gov

Laxmikant V. Saraf, Senior Research Scientist
(509) 376-2006, Laxmikant.Saraf@pnl.gov

V. Shutthanandan, Senior Research Scientist
(509) 376-2708, Shuttha@pnl.gov

Lisa Smith, Senior Administrative Secretary
(509) 376-1518, L.Smith@pnl.gov

Chongmin M. Wang, Senior Research Scientist
(509) 376-4292, Chongmin.Wang@pnl.gov

James M. Young, Science & Engineering Associate
(509) 376-2046, Jim.Young@pnl.gov

Matrixed Staff

Christopher L. Aardahl, Senior Research Engineer
Advanced Processing and Applications, Environmental Technology Directorate
(509) 376-7022, Christopher.Aardahl@pnl.gov

Michael L. Alexander, Senior Research Scientist
Chemical Sciences Division, Fundamental Science Directorate
(509) 376-1576, Michael.Alexander@pnl.gov

Donald R. Baer, Laboratory Fellow
Chemical Sciences Division, Fundamental Science Directorate
(509) 376-1609, Don.Baer@pnl.gov

Cynthia J. Bruckner-Lea, Staff Scientist
Chemical Sciences Division, Fundamental Science Directorate
(509) 376-2175, Cindy.Bruckner-Lea@pnl.gov

Paul E. Burrows, Laboratory Fellow
Polymer Multilayer Technology, Energy Science & Technology Directorate
(509) 375-5990, burrows@pnl.gov

Scott A. Chambers, Laboratory Fellow
Chemical Sciences Division, Fundamental Science Directorate
(509) 376-1776, Sa.Chambers@pnl.gov

Ya-Huei Chin, Senior Research Scientist
Chemical, Biological & Processing Group, Environmental Technology Directorate
(509) 376-0134, Ya-Huei.Chin@pnl.gov

Brian P. Dockendorff, Science & Engineering Associate
Chemical Sciences Division, Fundamental Science Directorate
(509) 376-3539, Brian.Dockendorff@pnl.gov

Alice Dohnalkova, Science & Engineering Associate
Microbiology, Fundamental Science Directorate
(509) 376-0692, Alice.Dohnalkova@pnl.gov

Timothy C. Droubay, Research Scientist
Chemical Sciences Division, Fundamental Science Directorate
(509) 376-7065, Tim.Droubay@pnl.gov

Todd R. Hart, Science & Engineering Associate
Chemical, Biological & Processing Group, Environmental Technology Directorate
(509) 376-4966, Todd.Hart@pnl.gov

Timothy L. Hubler, Senior Research Scientist
Chemical, Biological & Processing Group, Environmental Technology Directorate
(509) 376-0249, Tim.Hubler@pnl.gov

Jay Grate, Laboratory Fellow
Chemical Sciences Division, Fundamental Science Directorate
(509) 376-4242, JWGrate@pnl.gov

Mark R .Gross, Senior Research Engineer
Polymer Multilayer Technology, Energy Science & Technology Directorate
(509) 375-6880, Mark.Gross@pnl.gov

Michael A. Henderson, Staff Scientist
Chemical Sciences Division, Fundamental Science Directorate
(509) 376-2192, Ma.Henderson@pnl.gov

Weilin Jiang, Senior Research Scientist
Chemical Sciences Division, Fundamental Science Directorate
(509) 376-5471, Weilin.Jiang@pnl.gov

Do Huei Kim, Senior Research Scientist
Chemical Sciences Division, Fundamental Science Directorate
(509) 376-2633, Do.Kim@pnl.gov

Jungbae Kim, Senior Research Scientist
Chemical, Biological & Processing Group, Environmental Technology Directorate
(509) 376-4621, Jungbae.Kim@pnl.gov

Igor V. Lyubinetsky, Senior Research Scientist
Chemical Sciences Division, Fundamental Science Directorate
(509) 376-5220, Igor.Lyubinetsky@pnl.gov

Yuehe Lin, Senior Research Scientist
Chemical, Biological & Processing Group, Environmental Technology Directorate
(509) 376-0529, Yuehe.Lin@pnl.gov

Charles HF Peden, Laboratory Fellow
Chemical Sciences Division, Fundamental Science Directorate
(509) 376-1689, Chuck.Peden@pnl.gov

Janos Szanyi, Senior Research Scientist
Chemical Sciences Division, Fundamental Science Directorate
(509) 376-6466, Janos.Szanyi@pnl.gov

Yong Wang, Chief Scientist
Chemical, Biological & Processing Group, Environmental Technology Directorate
(509) 376-5117, Yong.Wang@pnl.gov

William J. Weber, Laboratory Fellow
Chemical Sciences Division, Fundamental Science Directorate
(509) 376-3644, Bill.Weber@pnl.gov